Mon. Not. R. Astron. Soc. **000**, 000–000 (0000) Printed 18 September 2012 (MN LaTeX style file v2.2)

The mass and angular momentum distribution of simulated massive galaxies to large radii

Xufen Wu[1,3], Ortwin Gerhard[1], Thorsten Naab[2], Ludwig Oser[2], Inma Martinez-Valpuesta[1], Michael Hilz[2], Eugene Churazov[2,4], Natalya Lyskova[2,4]
[1] *Max-Planck-Institut für Extraterrestrische Physik, Giessenbachstrasse, 85748 Garching, Germany*
[2] *Max-Planck-Institut für Astrophysik, Karl-Schwarzschild-Str. 1, 85741 Garching, Germany*
[3] *Argelander-Institut für Astronomie der Bonn Universität, Auf dem Hügel 71, 53121 Bonn, Germany*
[4] *Space Research Institute (IKI), Profsoyuznaya 84/32, Moscow 117997, Russia*

18 September 2012

ABSTRACT

We study the mass distributions, circular velocity curves (CVCs), line-of-sight kinematics and angular momenta out to many $\mathrm{R_e}$ for a sample of 42 cosmological zoom simulations of galaxies with stellar masses from $2.7 \times 10^{10} M_\odot$ to $4.8 \times 10^{11} M_\odot$. In order to reduce the particle noise at large radii, we temporally smooth the observables of the simulated galaxies in a static potential. The mass of the simulated galaxies is parametrised by the circular velocity at $r = 5\,\mathrm{R_e}$ where $\mathrm{R_e}$ is the projected stellar half mass radius within 10% $r_{\rm vir}$. We find: (i) The projected stellar density distributions at large radii can be well fitted by Sérsic functions. The Sérsic indices range from ~ 3 to ~ 13 and correlate with stellar mass and galaxy size (low n, low mass, small size). (ii) The dark matter halo density profiles are consistent with simple power-law models, corresponding to flat dark matter CVCs for lower-mass systems, and rising CVCs for high-mass halos. (iii) The massive systems have nearly flat total (luminous plus dark matter) CVCs at large radii, while the less massive systems have mildly decreasing CVCs. The slope of the circular velocity at large radii correlates with Sérsic index and circular velocity itself. (iv) The short axes of simulated galaxies and their host dark matter are well aligned and their short-to-long axis ratios are correlated. (v) Stellar root mean square velocity $v_{\rm rms}(R)$ profiles are slightly falling, consistent with planetary nebulae observations in the outer halos of most early-type galaxies (ETGs). There are no analogues in the simulated galaxies of the second group of ETGs with rapidly falling $v_{\rm rms}(R)$ profiles. (vi) The line-of-sight velocity fields $\bar{v}$ show that rotation properties at small and large radii are correlated. Most radial profiles for the cumulative specific angular momentum parameter $\lambda(R)$ are nearly flat or slightly rising, with values in [0.06, 0.75) from $2\,\mathrm{R_e}$ to $5\,\mathrm{R_e}$. There are a few cases for which the local $|\bar{v}|/\sigma(R)$ decreases at large R, and some with localalized maxima of specific angular momentum. These properties are consistent with observations of ETGs at large radii. (vii) Stellar mass, ellipticity at large radii $\epsilon(5\,\mathrm{R_e})$, and $\lambda(5\,\mathrm{R_e})$ are correlated: the more massive systems have less angular momentum and are rounder, as for observed ETGs.

Key words: galaxies: kinematics and dynamics - methods: N-body simulations - methods: numerical

1 INTRODUCTION

Recent observations and cosmological simulations suggests a two-phase formation scenario for massive early-type galaxies (ETGs), in which an early phase of rapid star formation driven by cold accretion and dissipative mergers is followed by a prolonged phase of mass accretion through gas-poor major and minor mergers. Observations have shown that a population of old, massive ($\sim 10^{11} M_\odot$) and red ETGs were already in place at redshifts $z = 2-3$ (e.g., Fontana et al. 2006; Ilbert et al. 2010; Cassata et al. 2011), and that these galaxies have sizes several times smaller and densities an order of magnitude higher than present-day ETGs of similar mass (e.g., Daddi et al. 2005; Trujillo et al. 2007; van Dokkum et al. 2010). Recent simulations have found that massive galaxies grow initially through rapid star formation fuelled by infall of cold gas at $z \gtrsim 2$, leading to an old population of 'in situ' stars. Subsequently, the simulated galaxies grow through minor mergers, accreting old stars formed in subunits outside the main galaxy halo. The accreted stars are preferentially added to the outer haloes of the host systems, leading to efficient size evolution (e.g., Naab et al. 2009; Oser et al. 2010; Feldmann et al. 2010; Hopkins et al. 2010; Johansson et al. 2012).

While there is relatively little stellar mass in the outer regions of ETGs at galactocentric radii $\gtrsim 2\,\mathrm{R_e}$, these stars may carry indispensable information about the late assembly history of the galaxies. With relaxation times in the present-day outer stellar halos of up to several Gyrs, the record of the recent halo accretion history may be relatively well preserved (van Dokkum 2005; Duc et al. 2011). The outer halo stars may also contain a significant fraction of the angular momentum of the galaxies (Romanowsky & Fall 2012), and they can be used as gravitational tracers to study the mass distribution, dark matter fraction and potential of ETGs at large radii. Therefore, a detailed investigation of the structure and kinematics of the outer stellar haloes, comparing simulated and observed halos, may reveal important information about the formation history of ETGs.

Traditional long slit measurements and more recent observations with integral-field units (IFUs) have provided detailed kinematic and dynamical information about the central regions of ETGs, $R \lesssim 1 - 2\,\mathrm{R_e}$ (e.g., Bender et al. 1994; Gerhard et al. 2001; Cappellari et al. 2006). Using 2-dimensional stellar kinematics from the SAURON IFU out to $\sim 1\,\mathrm{R_e}$, and a measure of the projected angular momentum condensed into the cumulative $\lambda(R)$ parameter, ETGs can be separated into two main groups, fast rotators (FR, $\lambda(R) \gtrsim 0.1$) and slow rotators (SR, $\lambda(R) \lesssim 0.1$ Emsellem et al. 2007, 2011). This division is part of a wider dichotomy between oblate-spheroidal disky, coreless, rotating ETGs with little radio and X-ray emission, and triaxial boxy, cored, non-rotating, radio-loud and X-ray bright systems (see Bender et al. 1989; Kormendy & Bender 1996; Kormendy et al. 2009).

In the outer halos, obtaining kinematic information is much harder because of the rapid decline of stellar surface brightness with radius. Most of the known kinematic properties come from observations of Planetary Nebulae (PNe) which have been found to be good tracers of the stars and can be observed up to $\sim 8\,\mathrm{R_e}$ (e.g., Méndez et al. 2001; Coccato et al. 2009; McNeil-Moylan et al. 2012). Recently, individual IFU pointings and slitlet masks have also been used at $3 - 4\,\mathrm{R_e}$ (Weijmans et al. 2009; Proctor et al. 2009; Murphy et al. 2011). The PNe observations show that the division between FR and SR is largely preserved to large radii, although there are also galaxies whose $\lambda(R)$-profiles drop significantly outwards, possibly implying that the high inner values are due to disks whose light contribution fades towards large radii. Most of the PNe RMS velocity profiles decrease slowly with radius, but a subset of galaxies show steep 'quasi-Keplerian' outer decreases of velocity dispersion (Coccato et al. 2009).

Analysis of outer stellar kinematics, strong lensing, and hydrostatic equilibrium of X-ray emitting hot gas shows that massive elliptical galaxies have nearly isothermal inner mass distributions, equivalent to flat circular velocity curves (e.g., Gerhard et al. 2001; Koopmans et al. 2006; Auger et al. 2010; Churazov et al. 2008, 2010; Nagino & Matsushita 2009). For the lower mass ellipticals, the situation is less clear, as the mass-anisotropy degeneracy is stronger for declining velocity dispersion profiles, their X-ray emission is too faint, and the lensing samples are dominated by massive systems. The dynamical modelling of integrated light and PNe indicates somewhat more diffuse dark matter halos in these galaxies (de Lorenzi et al. 2008, 2009; Napolitano et al. 2009). Another useful tracer of the outer mass distributions is the globular clusters (GCs); especially massive ellipticals contain large GC populations (e.g., Schuberth et al. 2010; Strader et al. 2011). However, a larger fraction of GCs may be recently accreted systems, as their relative frequency is tilted more towards small systems than that of PNe and light (Coccato et al. 2012).

The purpose of this paper is to analyze the mass distributions, outer kinematics, and angular momentum distributions of a representative sample of simulated massive galaxies, as a basis for comparison with kinematic observations and inferred mass distributions of nearby ETGs. We consider a sample of 42 resimulated galaxies from the high-resolution cosmological simulation of Oser et al. (2010), which grew through the two-phase processes of early in-situ formation followed by late accretion and minor mergers (Oser et al. 2012). The paper is organised as follows: In §2 we briefly describe the present-day (z=0) model galaxies extracted from the cosmological zoom simulations, and the method we use to derive smooth kinematic maps from their particle distributions. In §3, we study the mass density distributions of the stars and dark matter in these galaxies, as well as the corresponding circular velocity curves (CVCs). Then in §4, we investigate the observable kinematics in these systems out to large radii. We finally consider the cumulative and local angular momentum profiles $\lambda(R)$ and $|\bar{v}|/\sigma(R)$ for the stellar components in §5. We end by summarizing our results in §6.

2 THE SIMULATED GALAXIES AND THEIR KINEMATIC ANALYSIS

The "galaxies" studied here are extracted from the cosmological zoom simulations of Oser et al. (2010, 2012). These simulations were carried out with the following cosmological model parameters (in standard notation): $h = 0.72$, $\Lambda_b = 0.044$, $\Lambda_{\mathrm{DM}} = 0.216, \sigma_8 = 0.77$, and initial slope of power spectrum $n_s = 0.95$. First, dark matter-only initial conditions were evolved from $z = 43$ to $z = 0$, and selected individual halos were identified together with their virial radii $r_{\mathrm{vir}} \equiv r_{200}$. For this simulation, the softening radius was 2.52 kpc h^{-1}. Then these halos were traced back in time, and were replaced with high resolution gas and dark matter particles. The new halos were evolved again from $z = 43$ to the present day including prescriptions for star formation, supernova feedback, gas cooling and a redshift dependent UV background radiation.

From these high-resolution simulations, we here select 42 galaxies at z=0 which do not have massive satellites at this time. The selection is based on the circular velocity curves of these systems within 5 effective radii (5 $\mathrm{R_e}$); we require that the estimated fluctuations in the CVC induced by satellites are smaller than 2%. The final simulated galaxies have stellar masses ranging from $2.7\times10^{10} M_\odot$

to 4.8×10^{11} $M_{\odot}$ within 10% $r_{\rm vir}$. Their typical effective radii (defined as the half-light radius within 10% $r_{\rm vir}$ in the 2-dimensional projection) are $\mathrm{R_e} \simeq$ 2-6 kpc (Oser et al. 2010). For comparison, the co-moving softening lengths for stars and dark matter particles in the resimulations are 0.4 kpc h^{-1} and 0.89 kpc h^{-1}, so the stellar kinematics are resolved for $R > 0.5\,\mathrm{R_e}$ in the smallest systems, and for $R > 0.2\,\mathrm{R_e}$ in the large galaxies.

The star formation model used for the simulations presented here (see Oser et al. 2010 for all details) favours efficient star formation at high redshift leading to preferentially spheroidal systems with old stellar populations. The simulations do not produce supernova driven winds and a model for feedback from central AGN is not included. Therefore, the fraction of available baryons (in every halo) converted into stars of the central galaxies in the simulated mass range is typically two to three times higher than estimates from models matching observed galaxy mass functions to simulated halo mass functions (e.g., Guo et al. 2010; Moster et al. 2010; Behroozi et al. 2010; Yang et al. 2012). Possible physical processes responsible for this discrepancy are strong wind-driving feedback from SNII (e.g., Dekel & Silk 1986; Oppenheimer & Davé 2008; Governato et al. 2010; Dalla Vecchia & Schaye 2012) and/or feedback from super-massive black holes (e.g., Croton et al. 2006; Di Matteo et al. 2008; McCarthy et al. 2010; Teyssier et al. 2011).

Other simulations with similar specifications (weak supernova feedback and no AGN feedback) result in galaxies with photometric and kinematic properties similar to present day elliptical galaxies (Naab et al. 2007; Johansson et al. 2009; Naab et al. 2009; Feldmann et al. 2010; Johansson et al. 2012). The galaxies used here are in agreement with early-type scaling relations of mass with radius and stellar velocity dispersion. In addition, they have close to isothermal total mass distributions, similar to some observed ellipticals (e.g. Gerhard et al. 2001; Koopmans et al. 2006; Churazov et al. 2010; Barnabè et al. 2011), and their observed size evolution between $z \sim 2$ and $z = 0$ is in agreement with recent observational estimates (Oser et al. 2012).

In contrast to the central regions of the simulated galaxies which are well resolved, in their outer regions ($R > 2\,\mathrm{R_e}$) the particle noise can be substantial. In addition, although we have already removed systems having massive satellites, many smaller substructures are still present in the outer parts of the remaining galaxies. We have decided to smooth out these small substructures rather than taking them out one by one. However, we have tested in a few cases that the results with both approaches are very similar. To reduce fluctuations in the final velocity fields caused by either particle noise or small satellites, we use an N-body code (NMAGIC, implemented by de Lorenzi et al. 2007) to temporally smooth the system while integrating the orbits of the particles in the gravitational potential, for one circular orbit period at $10\,\mathrm{R_e}$ ($\sim 10\%$ $r_{\rm vir}$). Since the total mass in gas within 10% $r_{\rm vir}$ in these systems is small (it is one order of magnitude smaller than the mass of stars within 10% $r_{\rm vir}$ for all 42 galaxies), we simply fix the gas particles at their initial positions while integrating the stellar and dark matter particle orbits.

The NMAGIC code is a spherical harmonics code with a made-to-measure (M2M) algorithm (Syer & Tremaine 1996; de Lorenzi et al. 2007). Here we use it as a normal N-body code. The Poisson solver adopted in NMAGIC is a spherical harmonic expansion potential solver. It uses a radial grid binned logarithmically within maximum radius $r_{\rm max} = 500\,\mathrm{kpc}$, and there are 400 radial bins. The spherical harmonics expansion is carried to $l_{\rm max} = 16$. This does not resolve the small satellites, which are therefore conveniently smoothed out during the integration.

The potential and gravitational acceleration are computed at a sequence of time steps separated by

$$\mathrm{dts} = \frac{1}{1000}\frac{2\pi \times 10\,\mathrm{R_e}}{v_{\rm circ,10\,R_e}}, \qquad (1)$$

i.e., 1000 times in one circular orbit period for $r = 10\,\mathrm{R_e}$. During each interval dts the orbits of the particles are integrated with an adaptive leap-frog scheme. Kinematic line-of-sight (LOS) observables are projected on a two-dimensional polar grid with resolution $n_r \times n_\phi = 20 \times 30$ on a $(10\,\mathrm{R_e})^2$ region, and then these observables, Δ_j for the $j_{\rm th}$ grid cell, are time averaged by integrating (Syer & Tremaine 1996; de Lorenzi et al. 2007)

$$\tilde{\Delta}_j(t) = \alpha \int_0^\infty \Delta_j(t-\tau) e^{-\alpha\tau} d\tau, \qquad (2)$$

where the temporal smoothing parameter α is taken to be

$$\alpha \equiv \frac{5}{1000\,\mathrm{dts}}, \qquad (3)$$

so that the smoothing time is $\alpha^{-1} = 200\,\mathrm{dts}$. This procedure effectively smoothes over the particle noise for the observables in the sparse outer regions of the simulated galaxies. In a later section (§4), we will illustrate the effect of the particle noise and of the satellites on the projected kinematics for one snapshot and compare with the time averaged kinematics obtained by the procedure just described.

3 MASS DISTRIBUTIONS AND CIRCULAR VELOCITY CURVES

In this section, we investigate the stellar and dark matter density profiles of the simulated galaxies at z=0. We use the amplitude and slope of the circular velocity curve to characterize the mass distribution, and determine the fraction of dark matter at intermediate radii.

Figure 1 shows the three-dimensional volume density profiles for stars and dark matter, for radii greater than the respective softening radii for the star and dark matter particles. The densities shown are temporally smoothed as described above. We find for all model galaxies that the stellar components have steeply decreasing density profiles from $1\,\mathrm{R_e}$ to $6\,\mathrm{R_e}$, with small cores in the centres, while the dark matter halos have flatter density profiles. Since the high resolution re-simulations of individual halos include a variety of physical processes for the baryonic component, the dark matter density profiles are different from the simple NFW-like profiles (Navarro et al. 1996, 2010) found in simulations that only include dark matter.

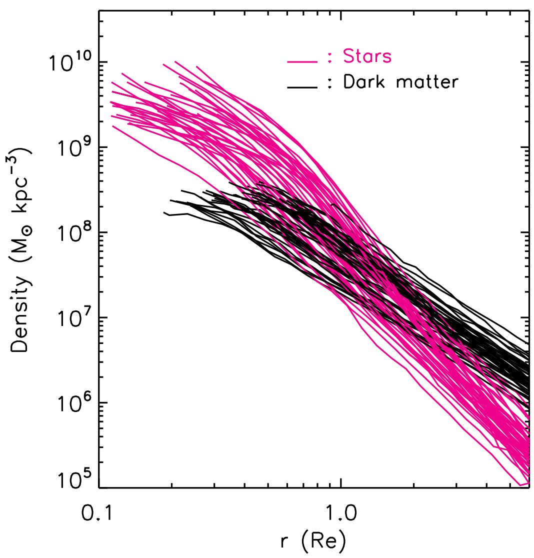

Figure 1. Temporally smoothed mass density profiles for stellar components (magenta lines) and dark matter halos (black) of the simulated galaxies. The profiles are shown as a function of normalized $r/\mathrm{R_e}$, extending from the softening length ($0.4h^{-1}$ kpc for stars and $0.89h^{-1}$ kpc for dark matter particles) to $6\,\mathrm{R_e}$.

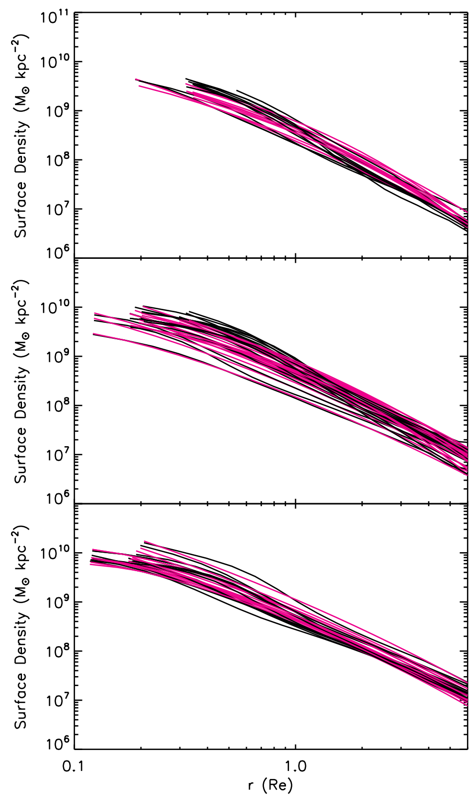

Figure 2. Temporally smoothed surface density profiles for the stellar components of the simulated galaxies (black lines), together with cored Sérsic fits (magenta lines), in bins of circular velocity at $5\,\mathrm{R_e}$. Upper panel: $v_{\rm circ}(5\,\mathrm{R_e}) < 220\,\mathrm{km\,s^{-1}}$, middle panel: $220\,\mathrm{km\,s^{-1}} < v_{\rm circ}(5\,\mathrm{R_e}) < 300\,\mathrm{km\,s^{-1}}$, lower panel: $v_{\rm circ}(5\,\mathrm{R_e}) > 300\,\mathrm{km\,s^{-1}}$).

3.1 Stellar density profiles

The surface density profiles of observed ETGs can be well fitted with a Sérsic profile (Sérsic 1963; Capaccioli 1989). Luminous ETGs have 'cored' profiles for which the slope of the central profile is below that of the outer Sércic profile (Trujillo et al. 2004). We therefore use a cored Sércic profile (Graham et al. 2003) to represent the stellar density of the model galaxies, using

$$I(R) = I_0 \exp\left\{-b_n\left[\left(\frac{R'}{R'_e}\right)^{1/n} - 1\right]\right\}, \qquad (4)$$

$$R' = \sqrt{R^2 + R_0^2}, \quad b_n = 1.9992n - 0.3271. \qquad (5)$$

Here n is the Sérsic index, I_0 is a normalization parameter related to the central surface density, and R'_e is a radius close to the effective radius if $R_0/R'_e \ll 1$ (because the relation used for $b_n(n)$ is for the original Sércic profile). To determine the parameters of the cored-Sérsic profile (I_0, n, R_0 and R'_e), we fit the density profile out to a truncation radius of $10\%\ r_{\rm vir} \sim 10\,\mathrm{R_e}$. The particles are binned on a logarithmic radial grid (see §2), and the surface densities are computed and temporally smoothed before fitting the model.

The cored-Sérsic model generally fits the particle distributions well, with a typical residual of $< 10\%$ of the local surface density. Values of the fitted parameters are given in Table 2 (columns 2-5) for all model galaxies (designation in column 1). We also list the proper effective (2D half-light) radius $\mathrm{R_e}$ for all stellar particles within $10\%\ r_{\rm vir}$ (column 6), which we take from Oser et al. (2010). We find that $\mathrm{R_e}$ is generally smaller than R'_e, with differences $\lesssim 20\%$ except for the two largest systems. Hereafter, we use $\mathrm{R_e}$ as length scaling unit. Fig. 2 shows the surface density of stellar particles (black lines) and their cored-Sérsic fits (magenta

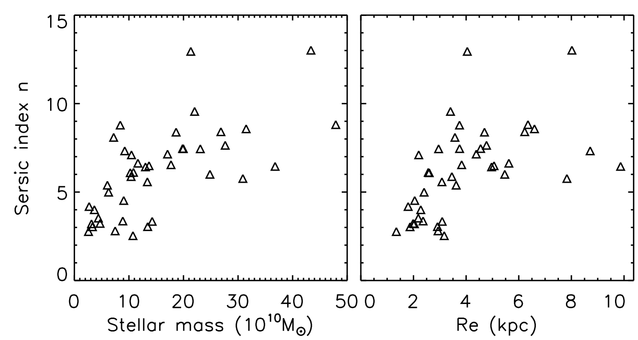

Figure 3. Relation between Sérsic index and stellar mass for the simulated galaxies (left panel), and relation between Sérsic index and effective radius (right panel).

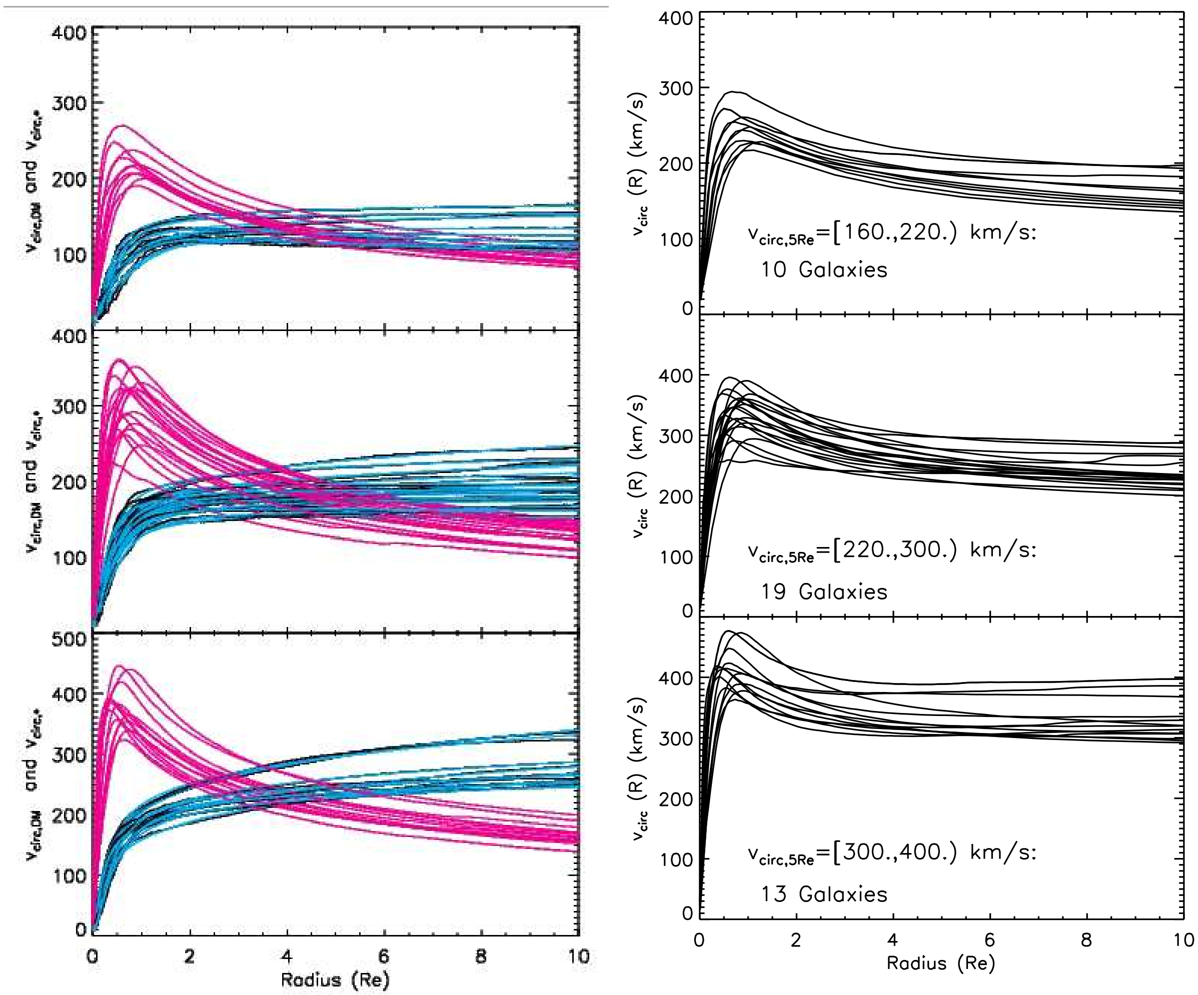

Figure 4. Left panels: Contribution to circular velocity curves (CVCs) from stars (magenta) and dark matter (black) for all model galaxies, separated in bins of increasing total circular velocity at $5\,R_e$, as given on the corresponding right panels. The cyan lines show the parameterised fits to the dark matter CVCs, using eq. 6. Massive halos with high v_{circ} have increasing dark matter CVCs (bottom panel), while low-mass halos have flat CVCs (top). Right panels: Total CVCs for all model galaxies: massive galaxies have flat total CVCs at large radii (bottom panel), while less massive galaxies (top) have mildly decreasing CVCs.

lines). The model galaxies in this figure are binned into three groups by mass, i.e., circular velocity at large radii ($5\,R_e$): $v_{circ,5\,R_e} = [160, 220), [220, 300), [300, 400)$ km s^{-1}; see below.

Interestingly, we find from Table 2 that model galaxies with larger stellar masses and effective radii have larger Sérsic indices, around $6-13$, while smaller galaxies have smaller Sérsic indices, around $3-6$. The left panel of Fig. 3 shows the relation between Sérsic index and stellar mass (within 10% r_{vir}) for all model galaxies. We indeed find a (weak) correlation between n and stellar mass as described. The right panel of Fig. 3 shows the relation between Sérsic index and size (i.e., R_e). Again we find a weak correlation, mostly for the smaller model galaxies; there is a substantial spread for the larger galaxies. This also implies that the sizes and stellar masses of the model galaxies are correlated. Both diagrams are also consistent with a bi-modal distribution; i.e., a different range of n for systems with effective radii $R_e < 3$ kpc and $R_e > 3$ kpc. In any case, systems with large R_e or stellar mass have on average shallower outer density slopes, i.e., more extended outer stellar halos. These relations between the Sérsic indices, stellar masses and sizes of the simulated galaxies are likely to be a consequence of the accretion-dominated (major and minor mergers) late assembly history of massive galaxies (Oser et al. 2012; Hilz et al. 2012). They appear qualitatively consistent with observations of ETGs (Caon et al. 1993; Prugniel & Simien 1997; Kormendy et al. 2009).

3.2 Dark matter mass distributions and circular velocity curves

The density profiles for the simulated dark matter halos, shown in Figure 1, are very similar to each other, with nearly the same slope between $1\,R_e$ and $6\,R_e$. To describe the mass distributions of the simulated galaxies more quantitatively, we study their circular velocity curves (CVCs) in Fig. 4. Here the circular velocity $v_{circ}(r) = [GM(r)/r]^{1/2}$ serves as a measure of the spherical part of the mass distribution, independent of the actual rotational velocities of the stellar or dark matter particles. The three rows of Fig. 4 show the model galaxy CVCs binned into three groups according to the value of $v_{\rm circ}$ at $5\,{\rm R_e}$ (for the binning the same ranges in $v_{\rm circ}$ are used as in Fig. 2). The left panels show the CVCs for the stellar components (magenta) and dark matter halos (black) separately. We see that the dark matter CVCs are nearly flat at large radii for the lowest $v_{\rm circ}$ bin, but increase outwards for higher mass systems (with high $v_{\rm circ}$). The figure also shows that the dark matter halos dominate the CVCs outside $4\,{\rm R_e}$.

The dark matter CVCs can be well approximated by power law mass distributions (potentials) within $10\,{\rm R_e}$. We use the following parametrisation:

$$v_{\rm circ}^{\rm DM} = \frac{v_0}{(5\,{\rm R_e})^a}\frac{r^{1.0+a}}{\sqrt{r_c^2+r^2}}, \tag{6}$$

Here v_0 is a normalization parameter for the circular velocity, r_c is the core radius of the dark halo, and a is the slope of the CVC at large radii. Columns 7-9 in Table 1 give the best-fitting values of v_0, a and r_c for the model dark matter halos. The values of r_c range between $1-2\,{\rm kpc}$ for almost all models, less than about twice the softening radius of the dark matter particles, $r_s^{\rm DM} = 0.89\ h^{-1}\,{\rm kpc}$, and the r_c do not correlate with the masses of the model galaxies. Therefore the presence of a core could be an effect of the softening in the simulations. In order to check this further, we also redid the fits while fixing $r_c = r_s^{\rm DM}$. The best-fitting CVCs obtained in this case are not significantly different from the previous CVCs (the typical residual is less than 1%). Considering the fact that $r_c/(5\,{\rm R_e}) \ll 1$ (Table 2), we see that the core radii do not significantly affect the rotation curves at $5\,{\rm R_e}$. Thus v_0 and a are approximately equal to the value and logarithmic slope of the dark matter CVC at $5\,{\rm R_e}$,

$$v_0 \simeq v_{\rm circ}^{\rm DM}(5\,{\rm R_e}), \qquad a \simeq S_5^{\rm DM} \equiv \frac{d\ln v_{\rm circ}^{\rm DM}}{d\ln r}(5\,{\rm R_e}). \tag{7}$$

The cyan lines in the left panels of Fig. 4 show the parameterised CVCs of the dark halo components. They agree well with the binned data for the halo circular velocities, especially at large radii (black lines).

The left panel of Fig. 5 quantifies the correlation between the outer slope $S_5^{\rm DM}$ of the dark matter CVC with the amplitude of the dark matter CVC at $5\,{\rm R_e}$ for the simulated galaxies. We find that for the low-$v_{\rm circ}^{\rm DM}(5\,{\rm R_e})$ systems the slopes of dark matter CVCs are around zero and for the high-$v_{\rm circ}^{\rm DM}(5\,{\rm R_e})$ systems these slopes are slightly above zero (<0.3), confirming the result from Fig. 4.

The right panels of Fig. 4 show the *total* CVCs of the model galaxies, including the contribution from the stars, which we parametrize again by their value and logarithmic slope at $5\,{\rm R_e}$,

$$v_{\rm circ}(5\,{\rm R_e}), \qquad S_5 \equiv \frac{d\ln v_{\rm circ}}{d\ln r}(5\,{\rm R_e}). \tag{8}$$

The total CVCs are slightly falling at large radii ($5\,{\rm R_e}$) for the systems in the upper right panel, whose $v_{\rm circ}(5\,{\rm R_e})$ is smaller than $220\,{\rm km\,s^{-1}}$, while they are nearly flat outside $2\,{\rm R_e}$ for the most massive model galaxies whose $v_{\rm circ}(5\,{\rm R_e})$ is larger than $300\,{\rm km\,s^{-1}}$ (lower right panel; see also Lyskova et al. 2012). The right panel of Fig. 5 quantifies

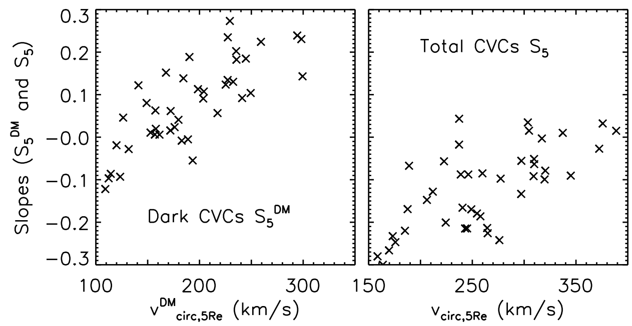

Figure 5. Left panel: The logarithmic slope of the dark matter CVCs for all model galaxies, versus their outer circular velocity, $v_{\rm circ}^{\rm DM}(5\,{\rm R_e})$. Right panel: The logarithmic slope of the total CVCs including stars and gas, versus total $v_{\rm circ}(5\,{\rm R_e})$. Massive galaxies (with large values of $v_{\rm circ}(5\,{\rm R_e})$) have zero slopes, i.e., flat CVCs, while smaller galaxies have CVC slopes between flat (0.0) and slightly falliing (-0.3).

this correlation by showing the total slopes S_5 versus the circular velocities at $5\,{\rm R_e}$. Model galaxies with larger values of $v_{\rm circ}(5\,{\rm R_e})$ have $S_5 \sim 0.0$, i.e., flat CVCs at large radii, while the remaining galaxies have slopes between $[0.0,\ -0.3]$, i.e., CVCs between flat (0.0) and mildly falling (-0.3).

Thus it is clear that the slope of the CVC at large radii is correlated with the amplitude of the circular velocity, and hence with model galaxy mass. The correlation is clearest for the dark matter halos alone (see left panel of Fig. 5 and Eq. 6), while it is weakened when the baryonic component is taken into account. All values for circular velocities and CVC slopes at $5\,{\rm R_e}$ can be found in Table 1.

The correlation between Sérsic index and stellar mass shown for the simulated galaxies in Fig. 3 suggests that also their total mass and hence circular velocity at large radius might correlate with the Sérsic index. The upper right panel of Fig. 6 confirms such a correlation between the total $v_{\rm circ}(5\,{\rm R_e})$ and Sérsic index n, but with broad spread. Model galaxies with smaller $v_{\rm circ}(5\,{\rm R_e})$ are on average more compact (have smaller n), while model galaxies with larger $v_{\rm circ}(5\,{\rm R_e})$ are more extended (have higher n).

Furthermore, since the circular velocity at large radius correlates with its own slope, there should be a correlation between the slope of the CVC and the Sérsic index. We see this correlation in the lower right panel of Fig. 6: Sérsic n increases with increasing slope of the CVC at large radii.

At large radii most simulated galaxies are dominated by dark matter; therefore, we expect that the circular velocities contributed by the dark matter halos also show these correlations. We show the relation between the Sérsic indices, $v_{\rm circ}^{\rm DM}$ at $5\,{\rm R_e}$, and the slope of $v_{\rm circ}^{\rm DM}(5\,{\rm R_e})$ in the left panels of Fig. 6 and find that these correlations also exist. In fact, they are slightly stronger than those obtained with the parameters of the total mass distribution which includes the stellar and remaining gaseous mass in the simulated galaxies.

Finally, we show the fraction of dark matter within 3-dimensional spheres of $1\,{\rm R_e}$ (left panel of Fig. 7) and $5\,{\rm R_e}$ (right panel) for the model galaxy sample. At $1\,{\rm R_e}$, the dark matter fractions are between $15\%-30\%$, i.e., the luminous matter dominates by a factor 3-7. At $5\,{\rm R_e}$, the dark matter fractions are between $40\%-65\%$, i.e., the amount of

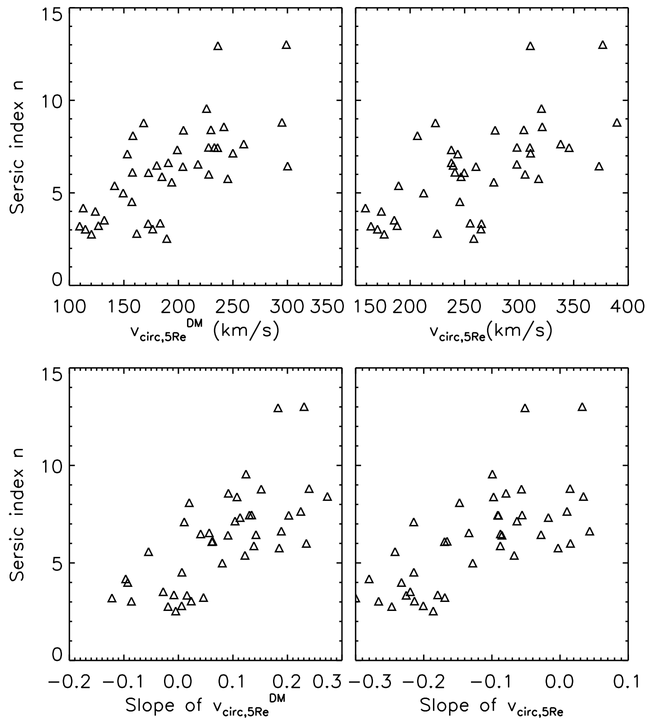

Figure 6. Relation between Sérsic index and circular velocity curve parameters for simulated galaxies. Sérsic index is plotted against circular velocity from dark matter only (upper left panel), slope of the dark matter CVC (lower left panel), total circular velocity (upper right panel), and slope of total CVC curve (lower right panel), all evaluated at $5\,\mathrm{R_e}$.

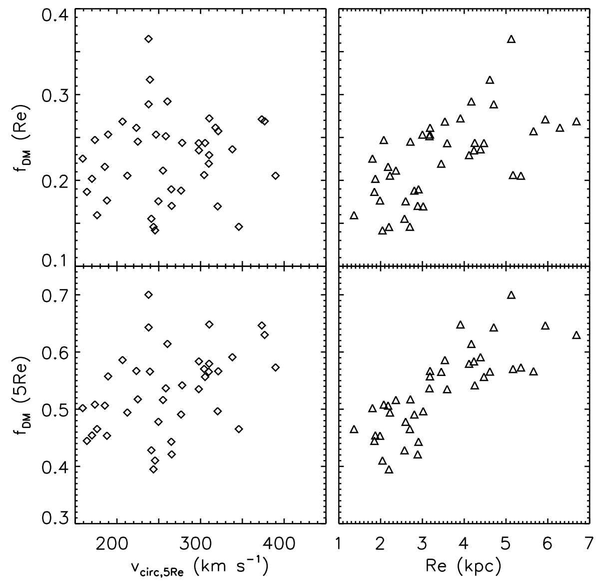

Figure 7. Dark matter fraction for all model galaxies at $1\,\mathrm{R_e}$ (upper panels) and $5\,\mathrm{R_e}$ (lower panels), versus outer circular velocity $v_{\rm circ}(5\,\mathrm{R_e})$ (left panels) and versus effective radius (right panels). Within $1\,\mathrm{R_e}$, the average mass in dark matter is about 25% of the total, while within $5\,\mathrm{R_e}$, the average dark matter fraction is slightly above 50%. The dark matter fraction has little (at $5\,\mathrm{R_e}$) to no dependence (at $1\,\mathrm{R_e}$) on circular velocity, but increases clearly with $\mathrm{R_e}$.

dark matter is now on average larger than the mass in stars. We can infer from Fig. 7 that the DM fraction increases with stellar mass (or circular velocity, or Sérsic n), and that this increase is mostly due to a dependence on effective radius rather than circular velocity (see also Hilz et al. 2012). These results are qualitatively consistent with dark matter fractions inferred from power-law dynamical modelling of PNe and GC observations (Deason et al. 2012) and strong lensing (Auger et al. 2010).

3.3 Shape correlation and alignment

Observed ETGs have ellipticities up to $\epsilon \simeq 0.8$ (Bernardi et al. 2003; Krajnović et al. 2011). The distribution of ellipticities depends on sample selection; it is approximately flat up to ellipiticity $\epsilon \simeq 0.7$ for the recent Atlas3D sample (see Krajnović et al. 2011, Fig.7). S0-like fast rotator ETGs are consistent with being a family of oblate systems viewed at random inclination angles, while slow rotator ETGs are moderately flattened ($\epsilon \simeq 0.3$) and often show kinematical misalignments, indicating that they are triaxial systems (Cappellari et al. 2007; Emsellem et al. 2011).

The shapes of the outer dark halos ($\gtrsim 10\%\ r_{\rm vir}$) can be estimated from the shear patterns in weak gravitational lensing data (Hoekstra et al. 2004; Mandelbaum et al. 2006; van Uitert et al. 2012). Some of these studies have found that the dark matter halos of red galaxies on scales beyond $\sim 0.1 r_{\rm vir}$ are preferentially aligned with the lens galaxies, but the signal is not as clear as might have been expected. Dark matter simulations predict that the halos are triaxial (Jing & Suto 2002; Allgood et al. 2006). In hydrodynamical simulations of disk galaxies, the inner halos become preferentially aligned with the disk and misaligned with the outer halos (Bailin et al. 2005; Bett et al. 2010; Hahn et al. 2010), while in binary major mergers the short axis of the stellar remnant is found to be oriented perpendicular to the long axis of the surrounding halo (Novak et al. 2006). It is therefore of interest to investigate the same question for the current model galaxies, which have a very different formation history.

To study the alignment of the simulated galaxies and their host dark matter halos, we determine the principal axis directions of both components at small radii ($2\,\mathrm{R_e}$) and large radii ($5\,\mathrm{R_e}$) at z=0. We find these quantities by diagonalising the moment of inertia tensor iteratively from all particles inside ellipsoids $x^2+(y/p)^2+(z/q)^2 = f^2\,\mathrm{R_e}^2$, where $f=1$ or 5, $p=b/a$, $q=c/a$ and, e.g., the latter is determined from $q \equiv c/a = \sqrt{\tilde{I}_{zz}/\tilde{I}_{xx}}$ where $\tilde{I}_{xx},\ \tilde{I}_{zz}$ are the diagonalised moments of inertia for all stellar particles within the ellipsoid. Because within $1\,\mathrm{R_e}$ there are only a few hundred dark matter particles for many of our models, we have chosen the inner radius at $2\,\mathrm{R_e}$ in order to ensure reliable results. The particle mass for the stellar component is $\sim 1/5$ of the dark matter particle mass, so there is a sufficient number of stellar particles even within quite small radii to define the shapes of the 'luminous' galaxies.

Figure 8 shows the histograms of misalignment angles

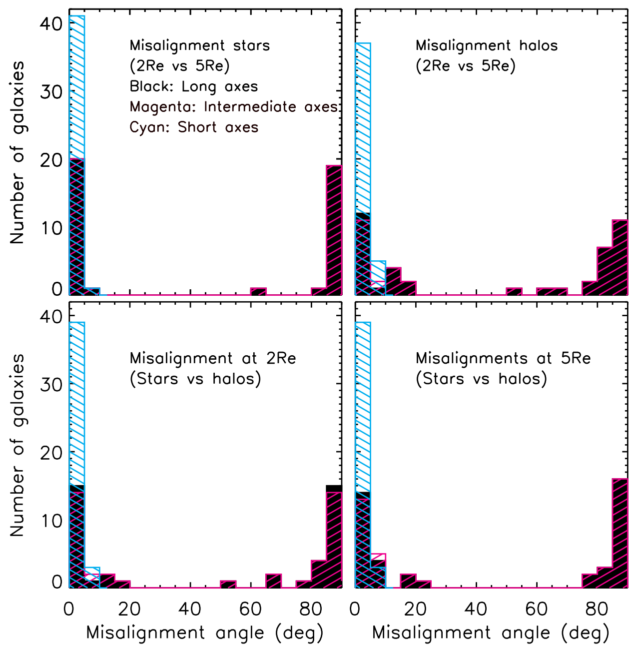

Figure 8. Alignment of the principal axes of the stellar and dark matter components. Histogram of misalignment angles for all 42 simulated galaxies, between: principal axes of the stellar component at $2\,\mathrm{R_e}$ and $5\,\mathrm{R_e}$ (top left); of the dark matter component at $2\,\mathrm{R_e}$ and $5\,\mathrm{R_e}$ (top right); of stars vs. dark matter at $2\,\mathrm{R_e}$ (bottom left); and stars vs. dark matter at $5\,\mathrm{R_e}$ (bottom right). Colours in each panel denote misalignment angle of the respective short axes (cyan), intermediate axes (magenta), and long axes (black).

between the short, intermediate, and long axes of the stellar and halo components at $2\,\mathrm{R_e}$ and $5\,\mathrm{R_e}$ for each component separately, and between both components. The short axes (blue) of the stars at different radii, the dark matter at different radii, and of the stars and dark matter distributions are always very well aligned (within $\lesssim 5°$). The long axes (black) and intermediate axes (purple) are approximately aligned within ($\lesssim 15°$) in about half of the cases; in the other half of the cases they are misaligned by roughly 90 degrees, meaning that the intermediate and long axes have switched between different radii or components. This can happen most easily when the system is nearly axisymmetric.

Figure 9 shows the short-to-long axis ratios of the dark matter halos versus those of the stars, at both $2\,\mathrm{R_e}$ and $5\,\mathrm{R_e}$. These axis ratios where obtained by viewing the system along the intermediate axis of the stellar component, and computing the projected axis ratio c/a from the diagonalized 2D projected moment of inertia tensor. At both $2\,\mathrm{R_e}$ and $5\,\mathrm{R_e}$, the axis-ratios of the galaxies are in the range [0.4,0.8] while the halos are slightly rounder, $c/a \in [0.5, 0.95]$. From the figure we see a moderately strong correlation between the shapes of the stellar and halo components, with scatter in the halo axis ratio at given stellar c/a of $\sim \pm 0.1$ at $5\,\mathrm{R_e}$ and $\sim \pm 0.2$ at $2\,\mathrm{R_e}$.

In summary, the short axes of the simulated galaxies and their host dark matter halos are well aligned within $\lesssim 5°$ througout the radial range probed ($2\,\mathrm{R_e}$-$5\,\mathrm{R_e}$), and

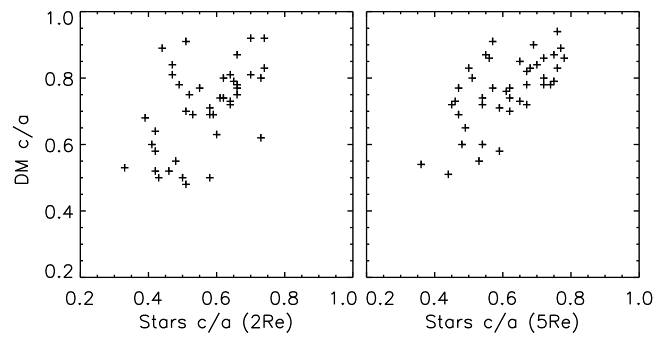

Figure 9. Short-to-long axis-ratios of stellar components versus halo components at $1\,\mathrm{R_e}$ (left) and $5\,\mathrm{R_e}$ (right). The c/a of stars and halos strongly correlate at large radii but not at small radii.

their shapes are correlated. Long and intermediate axes are either aligned or misaligned by 90°, i.e., switch their order, within slightly larger ($\lesssim 15°$) scatter.

4 LINE-OF-SIGHT KINEMATICS OF SIMULATED GALAXIES TO LARGE RADII

As is well-known, the outer kinematics of ETGs are difficult to measure because the stellar densities and surface brightness profiles decrease rapidly at large radii. The same problem also exists in the simulated galaxies where the particles follow similar density profiles. In addition to Poisson noise, there is also a further source of fluctuations that arises from various small satellites around the central galaxies.

In order to investigate the effects of the fluctuations from both low particle numbers and satellites, we consider three cosmological galaxies from our sample of Oser et al. (2010) more closely. These are denoted M0125, M1017, and M0300, and are selected based on their rotational properties (see also § 5). Velocity maps for these galaxies at $z = 0$ are shown in Fig. 10. The projection direction is along the intermediate axis of the stellar distribution within one effective radius[1]. The unsmoothed snapshot maps of mean LOS velocity $\bar{v}$ (upper panels in the left column of Fig. 10) show significant fluctuations. A map of the error $\delta\bar{v}$ in the mean LOS velocity is shown in the lower left panels of Fig. 10. This is defined as $\delta\bar{v}_j = \sigma_j/\sqrt{N_j}$, where σ_j and N_j are the velocity dispersion and number of particles in the $j_{\rm th}$ cell grid for this line-of-sight. Typical values for these fluctuations are $\delta\bar{v}_j = 20 - 80\ \mathrm{km\,s^{-1}}$. Model M1017 is an extreme case where the error can reach almost 50% of the mean LOS velocity itself.

In addition to the fluctuations caused by particle noise, these velocity maps show a number of well-defined substructures. These satellites will be moving along their own orbits until they finally merge with the central galaxy, and can locally have quite different LOS velocities from the host galaxy particles. Thereby the satellites change the 1-dimensional LOS velocity profiles and thus $\bar{v}$, and they may also affect the angular momentum profiles. We have decided not to

[1] The maps are interpolated from a polar grid as described in Sect. 2.

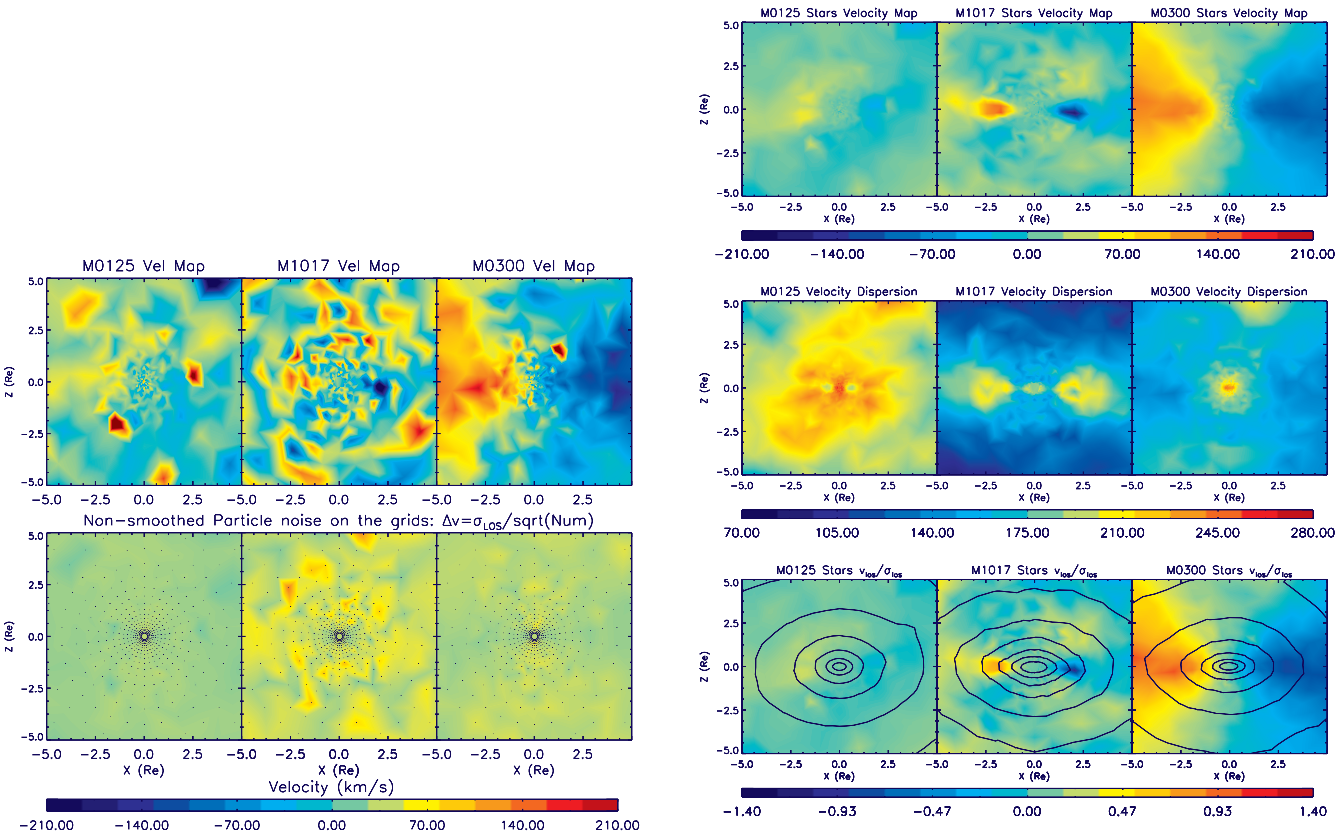

Figure 10. Edge-on LOS kinematics of selected model galaxies. Upper panels, left column: mean LOS velocity maps for the stellar components of three cosmological galaxies (labeled M0125, M1017, M0300), computed from the particle distributions for the snapshot at $z = 0$ (Oser et al. 2010). The maps are interpolated from a grid in radius and angle of $n_r \times n_\phi = 20 \times 30$ cells on a $(10\,\mathrm{R_e})^2$ region. Signatures from both particle noise and from a number of small substructures are visible. Lower panels, left column: particle noise error on the mean velocity for the same galaxies. The grid points (black dots) are overplotted. Upper panels, right column: Temporally smoothed mean LOS velocity maps ($\bar{v}$) for the stellar components of the same model galaxies. Middle panels, right column: Maps of temporally smoothed velocity dispersion σ. Bottom panels, right column: Maps of ratio $\bar{v}/\sigma$. The surface densities of the stellar components are overplotted on these maps; contour levels are $10^{7.0}$, $10^{7.5}$, $10^{8.0}$, $10^{8.5}$, $10^{9.0}$, $10^{9.5} M_\odot\,\mathrm{kpc}^2$. The three model galaxies chosen here are: a slow rotator (M0125), a slow rotator with a peak of $\lambda(R)$ around $2\,\mathrm{R_e}$ (M1017), and a fast rotator with increasing $\lambda(R)$ up to $2\,\mathrm{R_e}$ (M0300); see Sect. 5.

take all these small satellites out, but to consider the host galaxy after these substructures have phase-mixed away in its large-scale gravitational potential. The NMAGIC code used for this purpose (see Sect. 2) also computes a time average of the observables $\bar{v}$ and σ_j which allows us to obtain more reliable LOS kinematics at large radii than would otherwise be possible.

Recomputing in this way the projected LOS kinematics for the three galaxies in Fig. 10 results in the kinematic maps presented in the right column of Fig. 10. The three maps in the upper right panel are mean velocity maps $\bar{v}$. Fluctuations are greatly reduced compared to the unsmoothed maps in the left column. Also the fluctuations arising from the small satellites are mostly smoothed out. The middle panel in the right column of Fig. 10 shows maps of LOS velocity dispersion σ, and the lower panel shows maps of the ratio $\bar{v}/\sigma$ with overplotted stellar surface density contours.

For model M0125 (always in the left panels), the velocity field shows a mild rotation, and its velocity dispersion map shows large σ within $2.5\,\mathrm{R_e}$, implying that this galaxy is pressure-supported. For model M0300 (right panels), rapid disk-like rotation is seen from the mean velocity map, while σ is only large in the centre ($R < 0.5\,\mathrm{R_e}$); this object is significantly supported by rotation. Finally, in model M1017 (middle panels), one can see a hot disk-like structure at intermediate radii ($\sim 2.5\,\mathrm{R_e}$) in both the velocity and σ maps, while the rest of the galaxy has lower dispersion. Model M1017 is mostly pressure-supported with a rotationally supported component. While this model is somewhat unusual, the other two are quite typical for the large radius kinematics of fast and slow rotator galaxies in the simulated ETG sample. Observed outer velocity fields similar to the three cases shown here are those of NGC 5846 (a slow rotator galaxy), NGC 4564 (a fast rotator with a disk-like velocity field at intermediate radii; for both see Coccato et al. 2009), and NGC 1316 (a rapidly rotating merger remnant; see McNeil-Moylan et al. 2012).

Figure 11 shows line-of-sight velocity fields for 6 additional simulated galaxies out to $5\,\mathrm{R_e}$. These galaxies have been chosen as representatives for different dissipational and

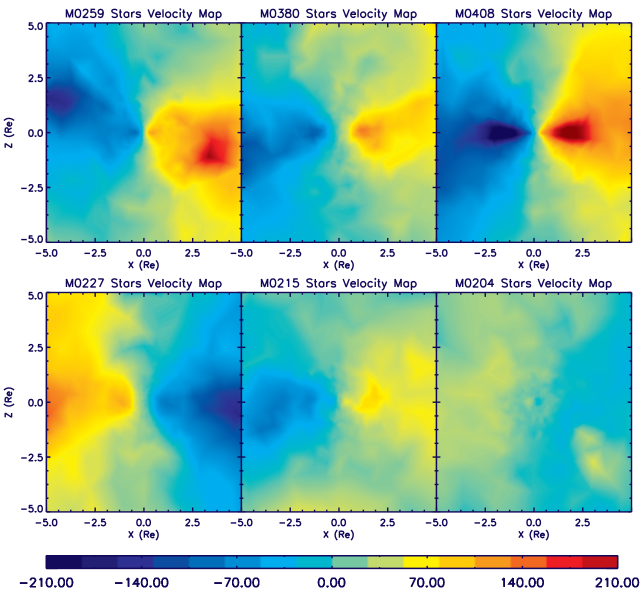

Figure 11. Edge-on mean LOS velocity maps for the stellar components of further 6 selected model galaxies. Upper panels show three simulated galaxies with large scale rotation. The galaxy in the top right panel has a pronounced disk component from a gas rich major merger. The lower panels show three simulated galaxies with a dissipationless merging history. The galaxy in the bottom right panel shows weak major and minor axis rotation; it has a formation history with many minor mergers.

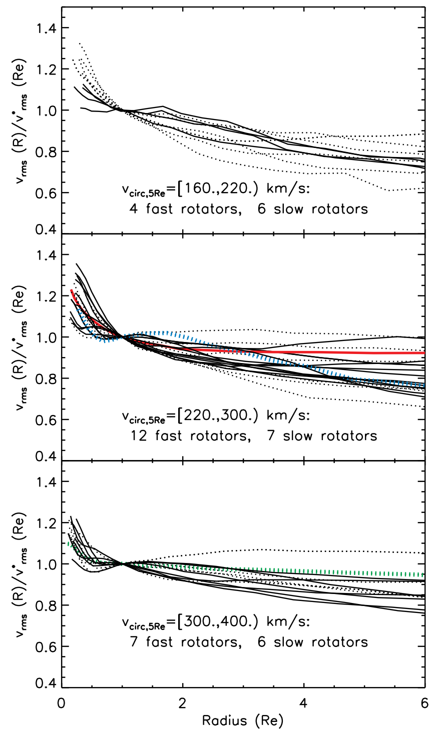

Figure 12. The root mean square velocities $v_{\rm rms}$ of the stellar components of 42 galaxies versus radius in bins of $v_{\rm circ,5\,R_e}$. The $v_{\rm rms}(R)$ profiles are normalized by their respective $v_{\rm rms}$ at $1\,{\rm R_e}$. Solid lines are for fast rotators while dotted lines are for the slow rotators; see Section 5. Coloured curves depict the three galaxies with velocity fields shown in Fig. 10: M0125 (green dotted line, bottom panel), M1017 (blue dotted line, middle panel), and M0300 (red solid line, middle panel).

dissipationless formation histories. For example, the galaxy in the top right panel has a pronounced disk component around $R \sim 2\,{\rm R_e}$ from a gas rich major merger, and the galaxy in the bottom right panel shows weak major and minor axis rotation; it has a formation history with many minor mergers. For further details about the formation histories of these simulated galaxies see Naab et al. (2012, in preparation).

4.1 Root Mean Square Velocity Profiles

Observations of outer ETG kinematics using planetary nebula velocities have shown that most ETGs are characterized by slowly declining profiles of circularly averaged RMS LOS velocity $v_{\rm rms}(R)$, but with a significant minority of galaxies for which the RMS velocity declines rapidly (Coccato et al. 2009). It is therefore of interest to investigate the equivalent radial profiles for the (re)simulated galaxies considered here.

Figure 12 shows the circularly averaged profiles of $v_{\rm rms}(R)$ for the 42 galaxies from Oser et al. (2010) in the three usual bins of $v_{\rm circ}(5\,{\rm R_e})$. The viewing direction for all simulated galaxies is edge-on along the intermediate axis of the stellar distribution. The $v_{\rm rms}(R)$ include projected rotation and velocity dispersion of all star particles, and are normalised by the respective values of $v_{\rm rms}(1\,{\rm R_e})$. We find that the $v_{\rm rms}(R)$ profiles decline moderately with radius for the low-mass systems, whereas they decrease only mildly for the high-mass systems. This is consistent with the CVCs shown in Fig. 4. The $v_{\rm rms}(R)$ profiles of fast and slow rotators (see Sect. 5) are not significantly different.

The $v_{\rm rms}(R)$ profiles in Fig. 12 are consistent with the major group in Coccato et al. (2009), but there is no equivalent in the simulations for the rapidly falling profiles shown in that paper (e.g., for NGC 3379). For this comparison, we also studied the $v_{\rm rms}(R)$ profiles of the simulated galaxies in face-on projection, with LOS parallel to the shortest axis. These face-on profiles are similar to those in edge-on projection. At least for the current sample of cosmological galaxies, the inclination angle does not seem to be an important parameter for $v_{\rm rms}(R)$. However, following the formation of thin disks is still problematic for such simulations, and this may also impact the geometric properties of merger remnants from such disks. Therefore this question should be revisited with future simulations once the disk problem has been solved.

4.2 Anisotropy profiles

In these cosmological simulations, the stars in the model galaxies have two origins: the inner in situ component forms at early times in a period of rapid star formation, while the second component stems from accreted stellar particles which is predominantly but not only found at large radii (Oser et al. 2010). The accreted component is characterized by radially anisotropic velocity dispersions (Abadi et al. 2006; Hilz et al. 2012) because the merging satellites come

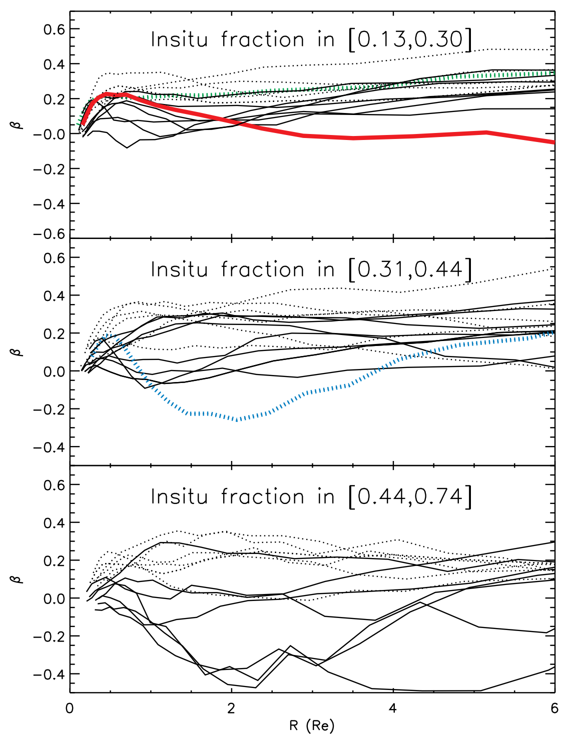

Figure 13. Velocity anisotropy profiles for the simulated galaxies in bins of in situ fraction of stars within $10\% r_{\rm vir}$. The coloured curves are as described in Fig. 12. Galaxies with low in situ fractions have more radially anisotropic orbit distributions, while tangential anisotropy is seen only for systems with high in situ fraction.

in on predominantly radial orbits, and so many of the stars stripped from the satellites enter the host galaxy on nearly radial orbits also.

Therefore, we would expect the kinematics of model galaxies to be more or less radially anisotropic depending on the relative fractions of in situ and accreted stars. Figure 13 shows anisotropy profiles $\beta(r) \equiv 1-(\sigma_\theta^2+\sigma_\phi^2)/2\sigma_r^2$ for all model galaxies, divided into bins of in situ fraction. As expected, tangentially anisotropic model galaxies can only be found in the group with large fraction of in situ stars (lower panel and also M1017 in the middle panel). Almost all simulated galaxies with low in situ star fraction (upper panel) are radially anisotropic with $\beta \simeq$ 0-0.3; but many of the systems with higher in situ fraction have similar anisotropies. As a result, there is no correlation between both quantities for the whole sample. We also find that slow rotators are radially anisotropic (except for M1017), while fast rotator model galaxies have both radially and tangentially biassed anisotropy profiles.

5 ANGULAR MOMENTUM PROFILES

To characterize the specific angular momentum of ETGs, Emsellem et al. (2007) introduced the $\lambda(R)$ profile $\lambda(R) =< Rv > / < R\sqrt{v^2+\sigma^2} >$, which is a luminosity-weighted, cumulative measure of projected angular momentum per unit mass within radius R. They found that ETGs can be divided into fast and slow rotators, according to whether $\lambda(R=R_e) > 0.1$ resp. < 0.1. Analyzing simulated merger remnants, Jesseit et al. (2009) found that $\lambda(R)$ is a good proxy for the true angular momentum of these remnants. Emsellem et al. (2011) revised the criterion for separating slow and fast rotators to include ellipticity values at R_e or $R_e/2$, and they also considered the effect of inclination and an assumed anisotropy on the resulting $\lambda(R)$ profile.

Much of the angular momentum of ETGs could reside at large radii, where kinematic measurements are more difficult than in the bright centers. Coccato et al. (2009) studied the kinematics of the outer halos of a sample of ETGs with PNe. They found (their Figure 14) that the $\lambda(R)$ profiles to large radii for the most part confirm the separation into fast and slow rotators based on the inner kinematics, but with some slow rotators having up to $\lambda(R) \sim 0.3$ at large R and some fast rotators whose $\lambda(R)$ profiles decrease outwards.

It is therefore of some interest to compare the specific angular momenta of the simulated galaxies with those of observed ETGs, out to several effective radii. To obtain an overview of the angular momentum properties of the simulated galaxies, we study the $\lambda(R)$ profiles for all the 42 cosmological galaxies, and to reach large radii we use the temporally smoothed observables (Sect. 2) in the computation of $\lambda(R)$,

$$\lambda(R_i) = \frac{\sum_{k=1}^{i}\sum_{j=1}^{N_\phi} m_{j,k}^P R_k |v_{j,k}|}{\sum_{k=1}^{i}\sum_{j=1}^{N_\phi} m_{j,k}^P R_k \sqrt{v_{j,k}^2+\sigma_{j,k}^2}}, \qquad (9)$$

where the summation is over the kinematic grid.

Figure 14 shows the resulting $\lambda(R)$ profiles, again with the simulated galaxies binned according to their outer circular velocity $v_{\rm circ,5\,R_e}$. The left panels of Fig. 14 show the $\lambda(R)$ profiles for edge-on view, while the right panels show the face-on $\lambda(R)$ profiles. Most of the simulated profiles have a very regular form, reaching a nearly constant value at $\sim 1-2R_e$, but some increase or decrease more noticeably at large radii. Both these variations and the general shapes of the $\lambda(R)$ profiles from the cosmological galaxies appear consistent with the observed $\lambda(R)$ profiles of ETGs to large radii, shown in Coccato et al. (2009). Their slopes at small radii appear somewhat shallower than the typical slopes seen in the SAURON and ATLAS^{3D} data (Emsellem et al. 2007, 2011).

To obtain a more detailed picture of the angular momentum in the outer stellar halos, it is useful to study the more local angular momentum parameter $|\bar{v}|/\sigma(R)$ as well. The local $|\bar{v}|/\sigma$ profiles for all simulated galaxies in edge-on view are shown in the middle panels of Fig. 14. For most simulated galaxies, the $|\bar{v}|/\sigma(R)$ profiles are nearly flat or increasing mildly with radius after reaching a plateau at $1-2R_e$. However, there are also a few exceptions for which $|\bar{v}|/\sigma(R)$ decreases at large R, and some with a strong local concentration of specific angular momentum. These features do not show up as well in the cumulative $\lambda(R)$ profiles.

As mentioned above, ETGs can be classified into fast and slow rotators according to their $\lambda(R)$ values at $\rm R_e$. For classifying the simulated galaxies we follow (Emsellem et al. 2007), taking $\lambda(\rm R_e) > 0.1$ to define fast rotators (solid lines in Fig. 14) and $\lambda(\rm R_e) < 0.1$ for slow rotators (dotted lines). The main reason for this choice is that this classification does not depend on ellipticity. We find that among 42 cos-

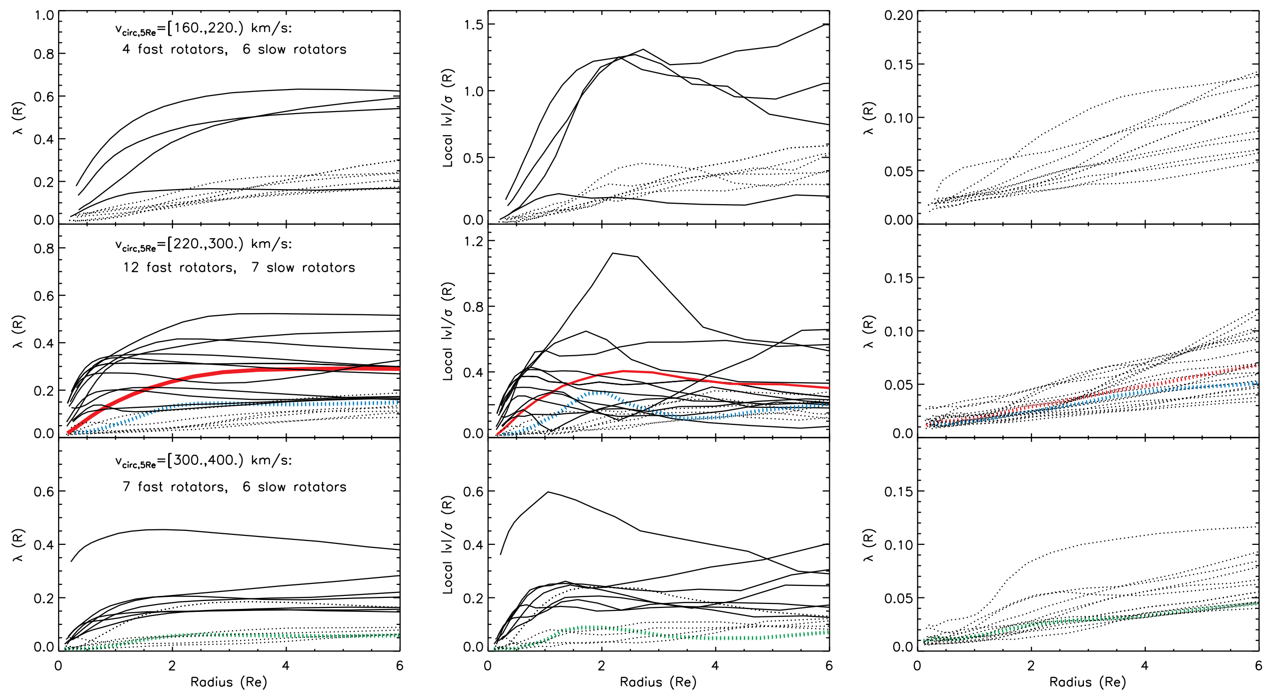

Figure 14. Specific angular momentum parameter $\lambda(R)$ profiles for the sample of 42 cosmological re-simulation galaxies, binned by circular velocity $v_{\rm circ}(5\,{\rm R_e})$ and plotted outside the softening radius $0.4/h$ kpc. Edge-on profiles (inclination $i = 90°$) are shown in the left panels and face-on profiles ($i = 0°$) in the right panels. The middle panels show $|\bar{v}|/\sigma$ profiles for $i = 90°$ in the same bins; these provide more local rather than cumulative information on the rotational properties. The solid lines are for fast rotators whereas the dotted lines show slow rotators; this classification depends on viewing angle. The coloured curves point to three typical galaxies: M0125 (green dotted lines on bottom panels), M1017 (blue dotted lines on middle panels) and M0300 (red solid lines on middle panels).

mological galaxies, 23 are fast rotators (based on the edge-on profiles) and 19 are slow rotators. The fraction of slow rotators is largest in the group of simulated galaxies with the highest circular velocities at $5R_e$. In the face-on view (right panels of Fig. 14), none of these systems rotates rapidly, and they are all classified as slow rotators. The fraction of slow rotators among the simulated galaxies (45%) is significantly more than in the ATLAS^{3d} sample (Emsellem et al. 2011); however, the sample selection criteria are not comparable (see Oser et al. 2010).

In Fig. 10 we showed the velocity fields of three typical galaxies: a slow rotator with very little rotation at any radii (M0125, left panels), a fast rotator for which rotation is significant at all radii (M0300, right panels), and a system rotating slowly in the inner $\rm R_e$ but rotating rapidly for $R \sim 2 - 4\,{\rm R_e}$ (M1017, middle panels). Especially the $\bar{v}/\sigma$ maps in Fig. 10 show the different rotational properties of these model galaxies well.

We use the same three simulated galaxies to show the beneficial effect of the temporal smoothing on the cumulative $\lambda(R)$ and local $|\bar{v}(R)|/\sigma$ profiles in Fig. 15, where the smoothed profiles from Fig. 14 are shown in red and the unsmoothed profiles are overplotted in black, for comparison. The upper panel shows that the amplitudes of the unsmoothed $\lambda(R)$ profiles are significantly higher than those of the time-smoothed counterparts. The lower panels show a similar effect in the local $|\bar{v}(R)|$ and $|\bar{v}|/\sigma(R)$ profiles; these have large fluctuations for a single snapshot, especially for the slow rotators, with values of up to a factor of 2 larger than in the smoothed profiles.

The reason for the higher amplitudes in the unsmoothed case lies in the definition of the $\lambda(R)$ parameters in terms of absolute values of mean velocity, so that negative and positive fluctuations cannot cancel in the angular or radial summation. The unsmoothed profiles can therefore be biased significantly by particle noise, especially for the slow rotators (such as model M0125) and in the center, and by global asymmetries (such as seen in model M0300 out to large radii). The light-blue curves in the top panel of Fig. 14 show the results of an additional test for this effect. They are determined from computing $\lambda(R)$ separately for the positive and negative velocity sides of the mean velocity maps in Fig. 10, but without the absolute value convention of eq. 9, and then adding the absolute $\lambda(R)$ values from both sides. This has the effect that positive and negative velocities on each side are allowed to cancel, which mimicks the effect of removing the noise or the asymmetry by the phase-mixing that occurs during temporal smoothing. It is clear from the Fig. 14 that the profiles obtained from this asymmetric averaging and from temporal smoothing agree closely with each other for all three simulated galaxies. This shows that to obtain a correct indication of the angular momentum of the system, the time averaging is necessary.

Returning to Fig. 14, it is clear that most of the simulated edge-on $\lambda(R)$ profiles are flat to slightly rising for $R \gtrsim 2\,{\rm R_e}$ (Figs. 14, 15). Thus, most fast rotators at R_e continue to rotate rapidly at large radii. Most of the slow

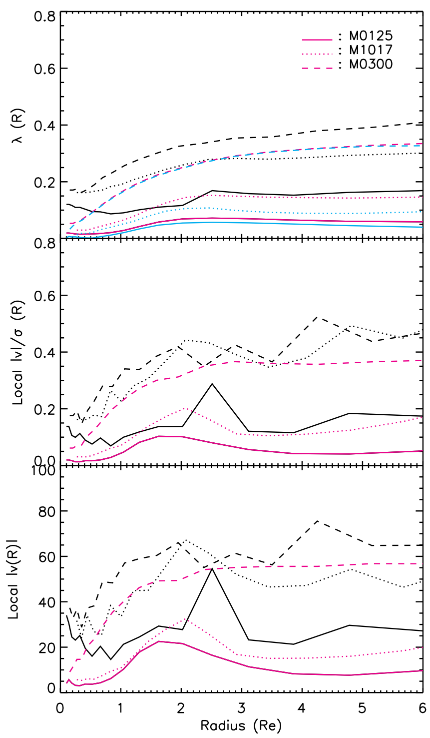

Figure 15. The 1-dimensional profiles of mean absolute velocity (lower panel), local rotation parameter $|\bar{v}(R)|/\sigma$ (middle), and cumulative specific angular momentum parameter $\lambda(R)$ (upper panel), for the three simulated galaxies M0125 (solid lines), M0300 (dashed lines) and M1017 (dotted lines). Black curves show profiles computed from unsmoothed data, magenta curves show the results based on temporally smoothed data, and light-blue curves show profiles based on two-sided averaging (see text).

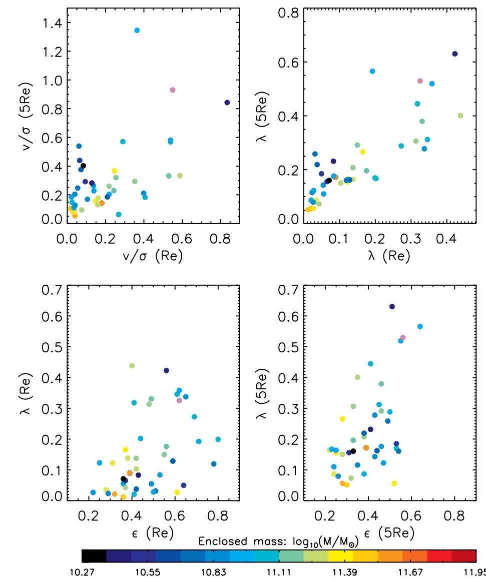

Figure 16. Relation between rotation, ellipticity and mass for outer stellar halos and central regions of the 42 simulated galaxies. Upper left panel: outer local $|\bar{v}|/\sigma$ ($5\,\mathrm{R_e}$) versus inner $|\bar{v}|/\sigma$ ($\mathrm{R_e}$) for edge-on view. Upper right panel: $\lambda(5\,\mathrm{R_e})$ versus $\lambda(\mathrm{R_e})$. Stellar halo rotation correlates with central rotation, especially for the flattest galaxies. Lower panels: $\lambda(R)$ versus ellipticity ϵ, at $\mathrm{R_e}$ (left) and $5\,\mathrm{R_e}$ (right), for edge-on view. The colour code in all panels shows stellar mass enclosed within 10% $r_{\rm vir}$. The more massive galaxies are rounder and have lower specific angular momenta, while the less massive galaxies are more evenly distributed in both parameters.

rotators have mildly increasing $\lambda(R)$ in the outer regions, especially for the group of less massive systems with circular velocities at large radii $< 220\,\mathrm{km\,s^{-1}}$. Fig. 16 confirms these trends. The upper left panel of Fig. 16 shows a correlation with much scatter between the central and outer local specific angular momentum, $|\bar{v}|/\sigma$ at $1\,\mathrm{R_e}$ and $5\,\mathrm{R_e}$. The upper right panel of Fig. 16 shows the close relation between the $\lambda(R)$ values at $1\,\mathrm{R_e}$ and $5\,\mathrm{R_e}$, consistent with the flat $\lambda(R)$ profiles. The correlation between the two $\lambda(R)$ values is stronger than for the local angular momentum parameters $|\bar{v}|/\sigma$ at the same radii, because of the cumulative nature of $\lambda(R)$ within radius R.

The $\lambda(R)$ profiles for a large number of nearby ETGs are shown out to $\lesssim 1.5\,\mathrm{R_e}$ in Figure 5 of Emsellem et al. (2011). More extended $\lambda(R)$ profiles for ETGs are shown in Proctor et al. (2009, out to 3 $\mathrm{R_e}$) and Coccato et al. (2009, out to 9 $\mathrm{R_e}$). Comparing with these observations, the $\lambda(R)$ profiles of our model galaxies are consistent with observed ETGs. Even for the unusual Model M1017, within $1.5\,\mathrm{R_e}$, there are similar $\lambda(R)$ profiles in Emsellem et al. (2011).

The observations of the SAURON (Cappellari et al. 2007) and ATLAS^{3d} projects (Emsellem et al. 2011) have shown evidence for correlations between specific angular momentum parameters (either $|\bar{v}|/\sigma$ or $\lambda(R)$ profiles) and ellipticity of these ETGs. To compare with these observations, we show in Figure 16 the $\lambda(R)$ parameters versus the ellipticities ϵ of the 42 simulated galaxies, both at $1\,\mathrm{R_e}$ (bottom left) and $5\,\mathrm{R_e}$ (bottom right). Here ellipticity $\epsilon \equiv 1 - c/a$, where a, c are the long and short semi-axes of the projected ellipse in edge-on projection (see §3.3). We list the values of ellipticity at $1\,\mathrm{R_e}$ and $5\,\mathrm{R_e}$ in columns 10 and 11 of Table 2, recalling that the central ellipticities for the lower mass systems have some uncertainty due to softening. Some of the galaxies contain highly flattened disk-like structures which result in large ellipticities at $R \sim \mathrm{R_e}$.

In general, the simulated slow rotators are rounder than the fast rotators, similar as in the observations. The distributions at $1\,\mathrm{R_e}$ and $5\,\mathrm{R_e}$ are similar, despite the already mentioned possibility that the ellipticity within $\mathrm{R_e}$ could be somewhat influenced by softening. The bottom left panel of Fig. 16 is in general agreement with the ATLAS^{3d} observations; however, the ellipticity range is narrower for the simulated galaxies. This is because the ATLAS^{3d} sample contains some very flat ETGs which may be disk galaxies, while our sample galaxies are mostly spheroidal galaxies.

The colour bar in Fig. 16 labels the stellar mass of the simulated galaxies within 10% $r_{\rm vir}$. This shows the correlations between angular momentum, ellipticity and stellar mass for the simulated galaxies: more massive galaxies rotate more slowly (have smaller $\lambda(R)$) and they are rounder, while the specific angular momenta for the less massive galaxies are spread over a wider range, in broad agreement with observations.

6 CONCLUSIONS AND DISCUSSION

In this work, we analyzed the structure and kinematics of 42 simulated galaxies from the cosmological re-simulations of Oser et al. (2010) which do not contain massive substructures at a level of $> 2\%$ perturbation in the CVC at redshift $z = 0$. Here we summarize and discuss our main results.

1. The stellar components of the model galaxies can be well fitted with cored Sérsic profiles. The Sérsic indices n correlate broadly with the stellar masses and sizes of the galaxies, with significant scatter, such that more massive galaxies have larger n, similar to observations of ETGs (e.g., Caon et al. 1993; Prugniel & Simien 1997; Kormendy et al. 2009).

2. Due to the interaction between dark matter and baryons during the assembly processes, the dark matter density profiles in the model galaxies deviate from the NFW-like profiles characteristic for dark matter only models (Navarro et al. 1996, 2010). The DM density slopes and the slopes of the DM CVCs are consistent with power laws and vary systematically with mass, such that the DM CVC is approximately flat (R^0) for less massive systems and slightly rising ($R^{0.3}$) for high mass galaxies.

3. The corresponding total CVCs are slightly falling ($R^{-0.3}$) for the less massive systems and approximately flat (R^0) for the more massive model galaxies. This is consistent with mass determinations for local galaxies (see the Introduction). As is then expected, galaxies with higher Sérsic indices n are found to have larger values of $v_{\rm circ}(5\,\rm R_e)$ and of the slope of the CVC at $5\,\rm R_e$. These outer parts of the cosmological galaxies are mostly dominated by their dark matter halos; so these trends hold also for the dark matter CVCs separately.

4. The short axes of the simulated galaxies and their host dark matter halos are well aligned within $\lesssim 5^\circ$ througout the radial range probed ($2\,\rm R_e$-$5\,\rm R_e$), and their shapes are correlated. Long and intermediate axes are either aligned or misaligned by 90°, i.e., switch their order, within slightly larger ($\lesssim 15^\circ$) scatter.

5. We computed mean velocity $\bar{v}$, velocity dispersion σ, and local $\bar{v}/\sigma$ fields out to $5\,\rm R_e$ for the simulated galaxies and illustrated their kinematic diversity for three of these. We temporally smoothed these velocity fields in order to suppress particle noise and fluctuations from small satellites and illustrate the necessity and effect of this in some detail. The simulated galaxy sample contains both purely dispersion-supported systems with no or little rotation, and objects that show disk-like rotation at a level of $v/\sigma \simeq 1$. We also show a rarer case with a disk-like structure at $\gtrsim 2.5\,\rm R_e$. The observed outer velocity fields of galaxies from PNe show a similar kinematic diversity.

6. Radial profiles of root mean square velocity $v_{\rm rms}(R)$ are slowly declining, independent of whether the simulated galaxies are fast or slow rotators, and similar for edge-on and face-on projections. These profiles resemble the majority group of outer $v_{\rm rms}(R)$ profiles determined in nearby ETGs from PNe velocities by Coccato et al. (2009); however, there are no analogues in the simulated galaxies for the rapidly falling $v_{\rm rms}(R)$ profiles seen in the observed sample. This could mean that these objects form through a channel different from the simulated galaxies studied here, or it could be related to the difficulty of modelling disk galaxies in the cosmological simulations; this issue requires further study.

7. Simulated galaxies with a large fraction of accreted stars are generally radially anisotropic. Only systems with dominant in situ fraction show tangential anisotropy. These trends are due to the fact that in the simulation the accreted stars are tidally dissolved from merging satellites on preferentially radial orbits. We also find that the slow rotators amongst the simulated galaxies are mostly radially anisotropic, while the fast rotators have both radial and tangential anisotropy profiles.

8. We determined cumulative $\lambda(R)$ and local $v/\sigma(R)$ angular momentum parameter profiles for the stellar components of all simulated galaxies from the time averaged velocity fields. For most simulated galaxies, the edge-on $\lambda(R)$-profiles are flat or slighty rising within $2\,\rm R_e - 6\,R_e$. Most fast rotators rotate fast at both small and large radii, but some have decreasing rotation at large radii. Lower mass slow rotators have mildly increasing $\lambda(R)$ with $\lambda(6\,\rm R_e) \in (0.1, 0.3]$, whereas high-mass slow rotators have flat $\lambda(R)$-profiles. Overall, λ increases with ellipticity, but with much scatter. These properties appear broadly consistent with those of observed ETGs.

7 ACKNOWLEDGMENTS

This project was mostly carried out while XW was as a postdoc in the dynamics group at MPE. During the final stages she acknowledges an Alexander von Humboldt fellowship at AIfA at Bonn University. We thank F. de Lorenzi, P. Das, and L. Morganti for their work and help with the NMAGIC code.

REFERENCES

Abadi M. G., Navarro J. F., Steinmetz M., 2006, MNRAS, 365, 747
Allgood B., Flores R. A., Primack J. R., Kravtsov A. V., Wechsler R. H., Faltenbacher A., Bullock J. S., 2006, MNRAS, 367, 1781
Auger M. W., Treu T., Bolton A. S., Gavazzi R., Koopmans L. V. E., Marshall P. J., Moustakas L. A., Burles S., 2010, ApJ, 724, 511
Bailin J., Kawata D., Gibson B. K., Steinmetz M., Navarro J. F., Brook C. B., Gill S. P. D., Ibata R. A., Knebe A., Lewis G. F., Okamoto T., 2005, ApJ, 627, L17
Barnabè M., Czoske O., Koopmans L. V. E., Treu T., Bolton A. S., 2011, MNRAS, 415, 2215
Behroozi P. S., Conroy C., Wechsler R. H., 2010, ApJ, 717, 379
Bender R., Saglia R. P., Gerhard O. E., 1994, MNRAS, 269, 785
Bender R., Surma P., Doebereiner S., Moellenhoff C., Madejsky R., 1989, A&A, 217, 35
Bernardi M., Sheth R. K., Annis J., Burles S., Finkbeiner D. P., Lupton R. H., Schlegel D. J., SubbaRao M., Bahcall N. A., Blakeslee J. P., Brinkmann J., Castander F. J., Connolly A. J., et al. 2003, AJ, 125, 1882
Bett P., Eke V., Frenk C. S., Jenkins A., Okamoto T., 2010, MNRAS, 404, 1137

Table 1. Stellar mass and circular velocity curves for the simulated galaxy sample: designations of the model galaxies (1*st* column), stellar mass within 10% $r_{\rm vir}$ (2*nd* column), circular velocities and their slopes at radius $5\,{\rm R_e}$ (3*rd* and 4*th* columns), circular velocities from dark halo components only and their corresponding slopes at $5\,{\rm R_e}$ (5*th* and 6*th* columns), parameters of the dark matter halo fit of eq. 6 (7*th* to 9*th* columns).

Model	Mass* ($10^{10} M_\odot$)	$v_{\rm circ,5\,R_e}$ ($\rm km\,s^{-1}$)	Slope of $v_{\rm circ,5\,R_e}$	$v^{\rm DM}_{\rm circ,5\,R_e}$ ($\rm km\,s^{-1}$)	Slope of $v^{\rm DM}_{\rm circ,5\,R_e}$	v_0 ($\rm km\,s^{-1}$)	a	r_c (kpc)
M0094	47.90	388.81	0.02	294.32	0.24	296.00	0.20	1.82
M0125	43.36	375.83	0.03	298.30	0.23	297.60	0.19	1.97
M0175	36.79	372.44	-0.03	299.45	0.14	296.18	0.16	2.02
M0190	31.48	320.43	-0.08	241.16	0.09	243.62	0.13	1.28
M0204	26.86	303.63	0.03	229.31	0.27	230.79	0.22	1.10
M0209	19.96	309.16	-0.09	232.47	0.13	236.07	0.06	2.44
M0215	27.64	337.30	0.01	259.32	0.22	261.00	0.14	1.84
M0224	24.84	304.75	0.02	227.34	0.23	230.15	0.14	0.95
M0227	30.88	317.13	-0.00	244.73	0.18	247.19	0.18	1.30
M0259	19.83	297.33	-0.06	227.16	0.13	226.97	0.12	1.73
M0290	22.04	319.75	-0.10	225.31	0.12	229.24	0.11	1.66
M0300	18.65	277.36	-0.10	204.18	0.11	207.10	0.09	1.37
M0329	21.34	309.59	-0.05	235.69	0.18	237.27	0.11	2.15
M0380	17.08	309.77	-0.06	249.41	0.10	248.51	0.09	2.03
M0408	17.71	297.20	-0.13	217.43	0.06	219.60	0.06	1.60
M0443	23.08	345.03	-0.09	235.38	0.20	237.56	0.09	1.57
M0549	11.64	237.34	0.04	190.32	0.19	189.23	0.13	1.07
M0616	13.03	259.79	-0.09	203.62	0.09	206.24	0.11	1.28
M0664	10.39	246.16	-0.09	184.48	0.14	187.15	0.07	1.36
M0721	13.37	276.12	-0.24	193.45	-0.05	198.68	-0.02	2.15
M0763	13.68	238.92	-0.09	179.72	0.04	183.14	0.01	1.79
M0858	14.26	264.88	-0.23	171.90	0.02	176.39	-0.01	2.03
M0908	13.43	264.42	-0.21	176.03	0.02	178.18	0.01	1.68
M0948	9.23	237.28	-0.02	198.55	0.11	197.98	0.10	1.96
M0959	8.41	222.72	-0.06	167.71	0.15	171.47	0.02	2.11
M1017	8.87	254.50	-0.18	182.86	-0.01	185.65	0.01	1.59
M1061	7.20	206.25	-0.15	157.89	0.02	159.55	0.04	1.72
M1071	10.82	240.60	-0.17	157.46	0.06	159.63	0.07	1.26
M1091	10.46	243.14	-0.21	152.81	0.01	155.36	-0.02	1.43
M1167	10.24	249.04	-0.17	172.19	0.06	173.63	0.04	1.56
M1192	6.05	189.01	-0.07	141.12	0.12	144.20	0.06	1.46
M1196	10.74	257.84	-0.19	188.89	-0.01	189.65	0.00	2.02
M1306	9.04	245.04	-0.21	156.97	0.01	160.81	0.01	1.52
M1646	7.47	224.42	-0.20	161.42	0.01	164.57	-0.02	1.80
M1859	6.27	211.94	-0.13	149.00	0.08	152.64	0.01	1.41
M2283	4.70	187.63	-0.17	126.38	0.05	128.99	-0.05	1.72
M2665	4.40	185.07	-0.22	131.70	-0.03	135.47	-0.02	1.84
M3431	2.59	175.82	-0.25	119.96	-0.02	125.09	-0.10	1.87
M3852	3.66	173.24	-0.23	123.50	-0.09	127.22	-0.15	1.97
M4323	3.31	169.72	-0.27	114.39	-0.09	116.01	-0.08	1.45
M5014	3.14	163.71	-0.30	109.17	-0.12	116.20	-0.15	2.41
M6782	2.71	158.66	-0.28	112.41	-0.10	116.33	-0.16	1.97

Caon N., Capaccioli M., D'Onofrio M., 1993, MNRAS, 265, 1013

Capaccioli M., 1989, in H. G. Corwin Jr. & L. Bottinelli ed., World of Galaxies (Le Monde des Galaxies) Photometry of early-type galaxies and the R exp 1/4 law. pp 208–227

Cappellari M., Bacon R., Bureau M., Damen M. C., Davies R. L., de Zeeuw P. T., Emsellem E., Falcón-Barroso J., Krajnović D., Kuntschner H., McDermid R. M., Peletier R. F., Sarzi M., van den Bosch R. C. E., van de Ven G., 2006, MNRAS, 366, 1126

Cappellari M., Emsellem E., Bacon R., Bureau M., Davies R. L., de Zeeuw P. T., Falcón-Barroso J., Krajnović D., Kuntschner H., McDermid R. M., Peletier R. F., Sarzi M., van den Bosch R. C. E., van de Ven G., 2007, MNRAS, 379, 418

Cassata P., Giavalisco M., Guo Y., Renzini A., Ferguson H., Koekemoer A. M., Salimbeni S., Scarlata C., Grogin N. A., Conselice C. J., Dahlen T., Lotz J. M., Dickinson M., Lin L., 2011, ApJ, 743, 96

Churazov E., Forman W., Vikhlinin A., Tremaine S., Gerhard O., Jones C., 2008, MNRAS, 388, 1062

Churazov E., Tremaine S., Forman W., Gerhard O., Das P., Vikhlinin A., Jones C., Böhringer H., Gebhardt K., 2010, MNRAS, 404, 1165

Coccato L., Gerhard O., Arnaboldi M., 2012, ArXiv e-prints

Table 2. Fit parameters for stellar surface density profiles, ellipticities, and rotation parameters for the simulated galaxy sample: designations of the model galaxies (1*st* column), best fit parameters for cored-Sérsic profiles: normalization parameter for central surface density, I_0, Sérsic index n, core radius R_0, effective radius R'_e (2*nd*-5*th* columns); the 6*th* column is $\mathrm{R_e}$ (i.e., the effective radius containing half the stellar mass within 10% $r_{\rm vir}$ from Oser et al. 2010); 7*th*-8*th* columns give ellipticities at $1\,\mathrm{R_e}$ and $5\,\mathrm{R_e}$ for the stellar mass distributions, 9*th* and 10*th* columns give rotation parameters $\lambda(5\,\mathrm{R_e})$, and ratio $v/\sigma(5\,\mathrm{R_e})/v/\sigma(\mathrm{R_e})$.

Model	I_0 ($10^8 M_\odot\,\mathrm{kpc}^{-2}$)	n	R_0 (kpc)	R'_e (kpc)	R_e (kpc)	ϵ ($\mathrm{R_e}$)	ϵ ($5\,\mathrm{R_e}$)	$\lambda(5\,\mathrm{R_e})$	$\frac{v}{\sigma}(5\,\mathrm{R_e})/\frac{v}{\sigma}(\mathrm{R_e})$
M0094	5.03	8.81	0.87	6.35	5.36	0.39	0.39	0.17	0.80
M0125	3.04	13.02	1.43	8.02	6.69	0.32	0.28	0.06	1.29
M0175	1.66	6.45	0.58	9.87	5.94	0.36	0.30	0.05	6.61
M0190	3.25	8.57	0.89	6.60	5.66	0.61	0.52	0.06	2.86
M0204	3.26	8.41	0.81	6.23	5.17	0.28	0.24	0.09	2.50
M0209	5.38	7.46	0.12	3.75	3.45	0.42	0.38	0.21	1.18
M0215	5.46	7.64	0.76	4.77	4.39	0.31	0.25	0.16	1.04
M0224	3.38	6.00	0.49	5.47	4.47	0.38	0.22	0.16	1.10
M0227	2.58	5.77	0.82	7.83	6.29	0.37	0.28	0.27	1.42
M0259	3.80	7.46	0.36	4.55	4.23	0.48	0.33	0.31	0.82
M0290	6.18	9.56	0.23	3.41	3.02	0.40	0.35	0.40	0.57
M0300	3.33	8.39	0.29	4.70	4.25	0.55	0.46	0.29	1.28
M0329	5.62	12.95	0.68	4.04	4.12	0.37	0.32	0.07	1.24
M0380	3.55	7.15	0.05	4.38	3.91	0.56	0.33	0.20	0.96
M0408	4.50	6.55	0.12	3.83	3.59	0.49	0.46	0.38	0.63
M0443	9.45	7.45	0.07	2.95	2.70	0.42	0.28	0.15	0.80
M0549	1.60	6.63	0.27	5.62	4.71	0.44	0.23	0.17	0.98
M0616	2.93	6.42	0.74	4.97	4.17	0.41	0.38	0.09	5.75
M0664	3.51	5.88	0.16	3.46	3.00	0.36	0.24	0.11	3.25
M0721	6.21	5.58	0.04	3.08	2.81	0.69	0.50	0.29	1.93
M0763	2.42	6.49	0.30	5.06	4.61	0.41	0.41	0.44	1.05
M0858	6.41	3.34	0.30	3.09	2.89	0.80	0.53	0.17	0.24
M0908	7.22	3.05	0.08	2.91	2.91	0.61	0.45	0.31	0.44
M0948	0.55	7.33	0.52	8.71	5.13	0.22	0.26	0.08	4.25
M0959	2.52	8.79	0.21	3.75	3.18	0.29	0.35	0.12	5.11
M1017	6.83	3.37	0.00	2.37	2.37	0.49	0.43	0.14	1.63
M1061	2.36	8.09	0.15	3.58	3.54	0.51	0.49	0.26	8.60
M1071	6.49	6.11	0.04	2.56	2.57	0.25	0.25	0.16	1.63
M1091	7.41	7.10	0.00	2.20	2.20	0.50	0.47	0.12	9.13
M1167	5.82	6.10	0.07	2.60	2.60	0.53	0.46	0.18	1.95
M1192	2.12	5.39	0.35	3.62	3.18	0.59	0.44	0.16	0.88
M1196	5.13	2.53	0.02	3.17	3.17	0.62	0.55	0.52	1.07
M1306	8.02	4.53	0.00	2.05	2.04	0.65	0.43	0.28	0.51
M1646	4.25	2.81	0.33	2.93	2.71	0.78	0.54	0.16	4.47
M1859	4.43	4.99	0.11	2.40	2.22	0.42	0.38	0.22	5.14
M2283	5.15	3.23	0.01	1.99	1.99	0.64	0.53	0.19	6.77
M2665	3.92	3.53	0.00	2.18	2.18	0.37	0.31	0.16	3.16
M3431	6.46	2.77	0.25	1.35	1.36	0.36	0.33	0.16	4.95
M3852	3.29	4.00	0.15	2.28	2.08	0.56	0.51	0.63	0.97
M4323	4.37	3.04	0.00	1.87	1.87	0.43	0.41	0.23	2.26
M5014	2.92	3.20	0.03	2.03	1.85	0.62	0.56	0.53	1.71
M6782	3.62	4.19	0.16	1.80	1.81	0.71	0.64	0.57	3.63

Coccato L., Gerhard O., Arnaboldi M., Das P., Douglas N. G., Kuijken K., Merrifield M. R., Napolitano N. R., Noordermeer E., Romanowsky A. J., Capaccioli M., Cortesi A., de Lorenzi F., Freeman K. C., 2009, MNRAS, 394, 1249

Croton D. J., Springel V., White S. D. M., De Lucia G., Frenk C. S., Gao L., Jenkins A., Kauffmann G., Navarro J. F., Yoshida N., 2006, MNRAS, 365, 11

Daddi E., Renzini A., Pirzkal N., Cimatti A., Malhotra S., Stiavelli M., Xu C., Pasquali A., Rhoads J. E., Brusa M., di Serego Alighieri S., Ferguson H. C., Koekemoer A. M., Moustakas L. A., Panagia N., Windhorst R. A., 2005, ApJ, 626, 680

Dalla Vecchia C., Schaye J., 2012, ArXiv e-prints

de Lorenzi F., Debattista V. P., Gerhard O., Sambhus N., 2007, MNRAS, 376, 71

de Lorenzi F., Gerhard O., Coccato L., Arnaboldi M., Capaccioli M., Douglas N. G., Freeman K. C., Kuijken K., Merrifield M. R., Napolitano N. R., Noordermeer E., Romanowsky A. J., Debattista V. P., 2009, MNRAS, 395, 76

de Lorenzi F., Gerhard O., Saglia R. P., Sambhus N., Debattista V. P., Pannella M., Méndez R. H., 2008, MNRAS, 385, 1729

Deason A. J., Belokurov V., Evans N. W., McCarthy I. G., 2012, ApJ, 748, 2

Dekel A., Silk J., 1986, ApJ, 303, 39

Di Matteo T., Colberg J., Springel V., Hernquist L., Sijacki D., 2008, ApJ, 676, 33

Duc P.-A., Cuillandre J.-C., Serra P., Michel-Dansac L., Ferriere E., Alatalo K., Blitz L., Bois M., Bournaud F., Bureau M., Cappellari M., Davies R. L., et al. 2011, MNRAS, 417, 863

Emsellem E., Cappellari M., Krajnović D., Alatalo K., Blitz L., Bois M., Bournaud F., Bureau M., et al. 2011, MNRAS, 414, 888

Emsellem E., Cappellari M., Krajnović D., van de Ven G., Bacon R., Bureau M., Davies R. L., de Zeeuw P. T., Falcón-Barroso J., Kuntschner H., McDermid R., Peletier R. F., Sarzi M., 2007, MNRAS, 379, 401

Feldmann R., Carollo C. M., Mayer L., Renzini A., Lake G., Quinn T., Stinson G. S., Yepes G., 2010, ApJ, 709, 218

Fontana A., Salimbeni S., Grazian A., Giallongo E., Pentericci L., Nonino M., Fontanot F., Menci N., Monaco P., Cristiani S., Vanzella E., de Santis C., Gallozzi S., 2006, A&A, 459, 745

Gerhard O., Kronawitter A., Saglia R. P., Bender R., 2001, AJ, 121, 1936

Governato F., Brook C., Mayer L., Brooks A., Rhee G., Wadsley J., Jonsson P., Willman B., Stinson G., Quinn T., Madau P., 2010, Nature, 463, 203

Graham A. W., Erwin P., Trujillo I., Asensio Ramos A., 2003, AJ, 125, 2951

Guo Q., White S., Li C., Boylan-Kolchin M., 2010, MNRAS, 404, 1111

Hahn O., Teyssier R., Carollo C. M., 2010, MNRAS, 405, 274

Hilz M., Naab T., Ostriker J. P., 2012, ArXiv e-prints

Hilz M., Naab T., Ostriker J. P., Thomas J., Burkert A., Jesseit R., 2012, ArXiv:1206.1597

Hoekstra H., Yee H. K. C., Gladders M. D., 2004, ApJ, 606, 67

Hopkins P. F., Bundy K., Hernquist L., Wuyts S., Cox T. J., 2010, MNRAS, 401, 1099

Ilbert O., Salvato M., Le Floc'h E., Aussel H., Capak P., McCracken H. J., Mobasher B., et al 2010, ApJ, 709, 644

Jesseit R., Cappellari M., Naab T., Emsellem E., Burkert A., 2009, MNRAS, 397, 1202

Jing Y. P., Suto Y., 2002, ApJ, 574, 538

Johansson P. H., Naab T., Ostriker J. P., 2009, ApJ, 697, L38

Johansson P. H., Naab T., Ostriker J. P., 2012, ApJ, 754, 115

Koopmans L. V. E., Treu T., Bolton A. S., Burles S., Moustakas L. A., 2006, ApJ, 649, 599

Kormendy J., Bender R., 1996, ApJ, 464, L119+

Kormendy J., Fisher D. B., Cornell M. E., Bender R., 2009, ApJS, 182, 216

Krajnović D., Emsellem E., Cappellari M., Alatalo K., Blitz L., Bois M., Bournaud F., Bureau M., et al. 2011, MNRAS, 414, 2923

Lyskova N., Churazov E., Zhuravleva I., Naab T., Oser L., Gerhard O., Wu X., 2012, MNRAS, 423, 1813

Mandelbaum R., Hirata C. M., Broderick T., Seljak U., Brinkmann J., 2006, MNRAS, 370, 1008

McCarthy I. G., Schaye J., Ponman T. J., Bower R. G., Booth C. M., Dalla Vecchia C., Crain R. A., Springel V., Theuns T., Wiersma R. P. C., 2010, MNRAS, 406, 822

McNeil-Moylan E. K., Freeman K. C., Arnaboldi M., Gerhard O. E., 2012, A&A, 539, A11

Méndez R. H., Riffeser A., Kudritzki R.-P., Matthias M., Freeman K. C., Arnaboldi M., Capaccioli M., Gerhard O. E., 2001, ApJ, 563, 135

Moster B. P., Somerville R. S., Maulbetsch C., van den Bosch F. C., Macciò A. V., Naab T., Oser L., 2010, ApJ, 710, 903

Murphy J. D., Gebhardt K., Adams J. J., 2011, ApJ, 729, 129

Naab T., Johansson P. H., Ostriker J. P., 2009, ApJ, 699, L178

Naab T., Johansson P. H., Ostriker J. P., Efstathiou G., 2007, ApJ, 658, 710

Nagino R., Matsushita K., 2009, A&A, 501, 157

Napolitano N. R., Romanowsky A. J., Coccato L., Capaccioli M., Douglas N. G., Noordermeer E., Gerhard O., Arnaboldi M., de Lorenzi F., Kuijken K., Merrifield M. R., O'Sullivan E., Cortesi A., Das P., Freeman K. C., 2009, MNRAS, 393, 329

Navarro J. F., Frenk C. S., White S. D. M., 1996, ApJ, 462, 563

Navarro J. F., Ludlow A., Springel V., Wang J., Vogelsberger M., White S. D. M., Jenkins A., Frenk C. S., Helmi A., 2010, MNRAS, 402, 21

Novak G. S., Cox T. J., Primack J. R., Jonsson P., Dekel A., 2006, ApJ, 646, L9

Oppenheimer B. D., Davé R., 2008, MNRAS, 387, 577

Oser L., Naab T., Ostriker J. P., Johansson P. H., 2012, ApJ, 744, 63

Oser L., Ostriker J. P., Naab T., Johansson P. H., Burkert A., 2010, ApJ, 725, 2312

Proctor R. N., Forbes D. A., Romanowsky A. J., Brodie J. P., Strader J., Spolaor M., Mendel J. T., Spitler L., 2009, MNRAS, 398, 91

Prugniel P., Simien F., 1997, A&A, 321, 111

Romanowsky A. J., Fall S. M., 2012, ArXiv e-prints

Schuberth Y., Richtler T., Hilker M., Dirsch B., Bassino L. P., Romanowsky A. J., Infante L., 2010, A&A, 513, A52

Sérsic J. L., 1963, Boletin de la Asociacion Argentina de Astronomia La Plata Argentina, 6, 41

Strader J., Romanowsky A. J., Brodie J. P., Spitler L. R., Beasley M. A., Arnold J. A., Tamura N., Sharples R. M., Arimoto N., 2011, ApJS, 197, 33

Syer D., Tremaine S., 1996, MNRAS, 282, 223

Teyssier R., Moore B., Martizzi D., Dubois Y., Mayer L., 2011, MNRAS, 414, 195

Trujillo I., Conselice C. J., Bundy K., Cooper M. C., Eisenhardt P., Ellis R. S., 2007, MNRAS, 382, 109

Trujillo I., Erwin P., Asensio Ramos A., Graham A. W., 2004, AJ, 127, 1917

van Dokkum P. G., 2005, AJ, 130, 2647

van Dokkum P. G., Whitaker K. E., Brammer G., Franx M., Kriek M., et al. 2010, ApJ, 709, 1018

van Uitert E., Hoekstra H., Schrabback T., Gilbank D. G., Gladders M. D., Yee H. K. C., 2012, ArXiv e-prints

Weijmans A.-M., Cappellari M., Bacon R., de Zeeuw P. T., Emsellem E., Falcón-Barroso J., Kuntschner H., McDer-

mid R. M., van den Bosch R. C. E., van de Ven G., 2009, MNRAS, 398, 561
Yang X., Mo H. J., van den Bosch F. C., Zhang Y., Han J., 2012, ApJ, 752, 41